D. Depla S. Mahieu

Editors

Reactive Sputter Deposition

With 341 Figures

Springer

Professor Dr. Diederik Depla
Dr. Stijn Mahieu
Gent University, Department of Solid-State Sciences
281-S1 Krijgslaan, 9000 Gent, Belgium
E-mail: diederik.depla@ugent.be, stijn.mahieu@ugent.be

ISSN 0933-033X

ISBN 978-3-540-76662-9 Springer Berlin Heidelberg New York

Library of Congress Control Number: 2007938637

Springer is a part of Springer Science+Business Media.
springer.com

Typesetting: Data prepared by SPi using a Springer LaTeX macro package
Cover concept: eStudio Calamar Steinen
Cover production: WMX Design GmbH, Heidelberg

Printed on acid-free paper SPIN: 12067657 57/3180/SPi 5 4 3 2 1 0

3

Modeling of the Magnetron Discharge

A. Bogaerts, I. Kolev, and G. Buyle

3.1 Introduction

Because of the industrial importance of sputter deposition magnetrons, there is a strong drive to simulate the entire magnetron deposition process, to replace trial-and-error experiments. This can lead to serious cost reduction, both for the manufacturers and the users of magnetron sputter equipment. The reasons are straightforward. For a typical coating plant, one of the main costs is the installation cost. Hence, it is a major advantage to have equipment that can realize a large throughput which fits specifications like required deposition speed, uniformity, reproducibility, or target lifetime. This means that magnetron manufacturers strive to a minimum "setup time," which requires from them the ability to predict whether the proposed design will work or not before the machine is actually built. This could be achieved by simulating the machines' characteristics. Of course, also the possibility of optimizing the deposition parameters without actually performing any real world experiment is attractive.

The ideal magnetron sputter deposition simulation would use as input the desired coating characteristics (e.g., electrical resistance, adhesion, refractive index, etc.) and process requirements (e.g., deposition speed, price per square meter, etc.). It would yield as output the necessary process parameters, e.g., sputter mode (DC, RF, pulsed, etc.), gas pressure, magnetic field strength, electrical power input, etc. In reality, we are still far away from such a model. The model becomes more realistic when the input and output are switched (see Fig. 3.1). In this way, the parameters defining the deposition process are the input; the deposited film properties form the output. Such model is referred to as a "virtual sputter magnetron." Efforts are made to develop such a simulation tool, e.g., [1–4].

Now, we will consider the virtual sputter magnetron of Fig. 3.1 in more detail. Basically, it consists of the following modules:

- Magnetic field modeling
- Magnetron discharge modeling

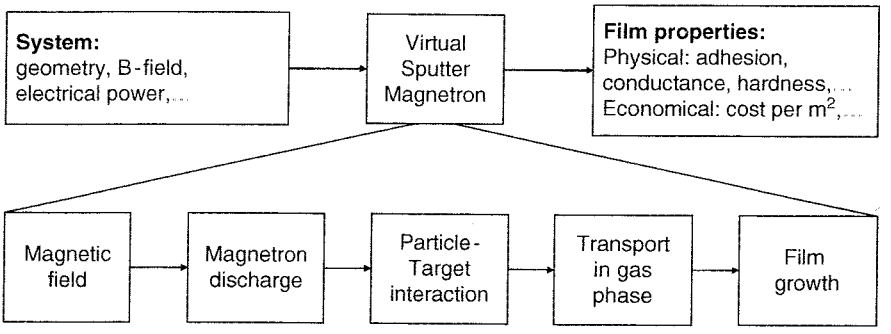

Fig. 3.1. Sketch of a virtual sputter magnetron, a simulation tool that would allow simulating the entire magnetron sputter-deposition process. The basic parts needed in such a tool are also shown

- Particle–target interaction, sputtering
- Transport of the sputtered particles through the gas phase
- Deposition and film growth at the substrate

From a scientific view-point, these modules cover a wide range of disciplines (plasma physics, surface physics, materials science, etc.). Some of the modules can be considered as known physics, others as challenging research topics. An example of the latter is the relation between the particles arriving at the substrate and the properties of the deposited film.

An accurate self-consistent virtual sputter magnetron that can operate over a wide range of parameters requires careful treatment of each of these modules. Like in a chain, the weakest link will determine the total strength: no matter how good the other modules, if there is one in the global model that is not accurate, the outcome of the whole model will be affected.

In the following, the different parts will be very briefly discussed and references to some relevant literature will be given.

3.1.1 The Magnetic Field

Essential for a magnetron discharge is of course the magnetic field. Hence, it is necessary for any simulation to have accurate values for the magnetic field. This can be achieved for the most complex magnetic configurations with high accuracy by using finite element models that are available as commercial packages or as free- or shareware. Packages reported in the literature regarding magnetron sputtering simulation are, e.g., POISSON [5, 6], OPERA [7], FEMME [8] or ELF/MAGIC [9]. A disadvantage of this method is that a high accuracy is only reached for a very dense mesh, which makes the magnetic field calculation time consuming. Very high accuracy is needed, however. Indeed, the length scale over which the electrons move during a time step when retracing their orbits is very small, in the order of 0.1 mm or less. For an accurate

simulation of the electron orbits, the magnetic field must vary smoothly over this scale length.

Another possibility is to calculate the magnetic field analytically. This has the major advantage that the field strength can be determined almost instantaneously at any point in space, which guarantees the smooth variation of the magnetic field along an electron orbit. Drawback is that only relatively simple magnetic configurations can be modeled and that the effect of magnetic shunts or complex magnet shapes cannot be dealt with.

The last possibility is to start from a measured magnetic field and interpolating or fitting it by an analytical expression. This also leads to a smooth spatial variation of the magnetic field. Of course, in such an approach the principle of virtual coater is violated: it does not allow simulating different magnetic field configurations, unless they are built in reality and measured accurately.

3.1.2 The Magnetron Discharge

The simulation of the magnetron discharge, based on the magnetic field, the gas pressure, and the electrical power input, is the next step. The underlying basic physics is at microscopic level "only" the motion of charged particles in a region subjected to an electric and magnetic field. This, combined with the necessary cross sections and electron yields, is in principle sufficient to describe the magnetron discharge. However, the emerging behavior of the plasma as a whole can be very complicated and turns this module of the virtual coater into one of the most difficult hurdles to take. Indeed, the small timescales required for the electron motion (10^{-11}–10^{-12} s) combined with the large timescales required for reaching equilibrium (10^{-5} s) make the computational load of numerical modeling extremely, and for certain configurations even unrealistically, high (see also Sect. 3.2 below). As the magnetron discharge is in principle the heart of the process, it is surprising that the more advanced simulation of the sputter process presented in [2] can completely bypass this and the previous module. Instead, the simulation starts with a profile characterizing the sputtered particles.

This module of the virtual sputter magnetron will be dealt with more extensively in Sect. 3.2, where the different modeling approaches and their specific (dis)advantages will be discussed. Also the rest of the chapter will be devoted specifically to the magnetron discharge modeling.

3.1.3 The Particle–Target Interaction

The sputtering process is based on the removal of target atoms by ion bombardment. The simulation of ion bombardment on a solid is well developed. These packages do not only allow determination of the sputter yield, i.e., the average number of atoms removed per incoming ion, but are also able to reproduce the angular and energy distribution of the atoms that leave the

surface. Very well known are Monte Carlo (MC) codes, such as TRIM [10,11], SRIM [12], and packages based on these. These packages have as main shortcoming that they are not dynamical, i.e., changes in the solid because of the incoming ion flux are not taken into account. Packages that take this into account are for instance TRIDYN [13,14] and KALYPSO [15]. Another MC simulation package on sputtering is ACAT [16]. All the mentioned packages are numerical simulations, implying that the computational load is heavy. This is especially true for the dynamical codes.

Hence, efforts are made to determine properties like the sputter yield and the angular and energy distributions of the sputtered particles by analytical expressions. These analytical expressions can be purely empirical or can be based on a simplified model. For the sputter yield, an example of an empirical expression is the well-known formula of Matsunami [17], whereas an example of a simplified model is the work reported in [18]. Also for the energy and angular distribution of the sputtered particles analytical models exist. A nice overview of this issue can be found in [19].

3.1.4 Particle Transport in the Gas Phase

Once the particles are sputtered from the target, they start spreading out through the vacuum chamber. The collision dynamics of these rather low energy (typically some tens of eV or below) particles are known. However, discussion exists about which interatomic potential is to be used [20]. This is not an academic discussion as the choice of the interatomic potential influences the simulated energy and angular distribution of the sputtered particles at the substrate [21]. As such, the exact potential is required for realistic thin film growth models. Ideally, the sputtered particle transport is described by combining a MC based model (for nonthermalized particles) and a diffusion model (for thermalized particles) [22].

In [23] the transport is described by a MC approach (SIMSPUD) and by a diffusion approach. Also in [24] a MC model is described. In [25] the film thickness distribution is simulated using a MC model for different target materials and for different target-substrate distances at different pressures. The results agree well with the experimental results, even for conditions where the ratio of the substrate and target diameter is large. Of course, also for this aspect of the magnetron sputter process simplified models have been developed, e.g., [26]. More information on simulations for particle–target interaction and particle transport in the gas phase can be found in the chapter "Transport of sputtered particles through the gas phase" by S. Mahieu et al.

3.1.5 Film Growth on the Substrate

For this part, the input consists of the energy and angular distribution of the particles arriving at the substrate and their arrival rate. With "particles" is not only meant the sputtered particles but also the electrons and discharge

gas particles (neutrals and ions) as they also contribute to the energy deposition at the substrate. The relation between this input and the resulting film properties is one of the more difficult parts when modeling the magnetron sputter process.

A first step is the simulation of the film thickness distribution and/or its deposition rate, as this follows rather straightforwardly from the information about the incoming particles and the sticking coefficients. In practice, in a lot of cases only this aspect is considered.

A more advanced form of this is "feature scale modeling." In microelectronics, the deposited coating might be required to fill structures like a thin trench or via. Feature modeling tries to simulate the exact coating thickness on all surfaces of such a feature [27–31].

One step further is to actually simulate the microstructure of the deposited material. The most accurate simulations are based on molecular dynamics, but this is extremely computationally intensive. Consequently, (empirical) approximations are needed. A sound discussion of this problem together with some examples of predicted structures can be found in [32]. In [33] the deposition on grain boundaries was simulated for Ti. Examples of the microstructural evolution during film growth (and the kinetic MC simulation thereof) can be found in [34]. Of course, also simplified models are developed, e.g., for the biaxial alignment in yttria-stabilized zirconia layers [35].

3.2 Overview of Different Modeling Approaches for Magnetron Discharges

The term numerical modeling refers to the process of finding approximate numerical solutions to a system of proper physical equations that adequately describe the system of interest. In a slightly broader aspect, also analytical models fall in this category. The latter are based on simplifications of globally valid, but complicated physical equations, rather than on numerical solutions of these globally valid equations. The choice of the proper set of equations is normally based on the given operating conditions. In other words, certain physical approximations are assumed already prior to the process of numerical solving, which in its turn introduces mathematical (numerical) approximations. The overall goal is always to obtain the most useful results at the lowest possible computational price.

A complete model of a magnetron discharge must include the magnetron plasma and its interactions with (some of) the solid surfaces that surround it. There are two surfaces that cannot be omitted in a model. These are the cathode (also known as target) and the substrate where the film is deposited. In many cases, the substrate is grounded, and therefore, acts as an anode. An intrinsic part of the operation of the magnetron is the effective electric field that results from the external power source and the movement of the plasma charged particles. Therefore, a procedure that calculates this field

should also be a part of the model. When the calculation of the resulting electric field is included in the model, the model is called self-consistent. It should be mentioned that for real self-consistency, some external electrical circuit should be coupled to the magnetron plasma [36–39]. However in the literature, it is common to use the term self-consistent even when no external circuit is included.

The existing models of magnetrons can be classified in several ways. The first division is between analytical and numerical models. The numerical models can further be split into fluid or kinetic models. The latter (i.e., kinetic) models can be based on numerical solutions of the Boltzmann equation, or on Monte Carlo (MC) simulations, also called particle simulations. These models are, however, not self-consistent, and need to be combined with a solution of the Poisson equation, resulting in either hybrid models or PIC-MCC simulations. In following sections, a literature overview of these different modeling approaches will be given.

3.2.1 Analytical Models

Analytical models (e.g., [40–57]) usually approximate the magnetron chamber with a one-dimensional (or sometimes even zero-dimensional) domain in the coordinate space, where the electric and magnetic forces are perpendicular to each other and the electron transport is considered in the direction parallel to the electric field and perpendicular to the magnetic field. In addition, the magnetic field is considered constant. Such a picture results, however, in a particularly simple form of the electron transport coefficients. Indeed, only the diagonal elements of the tensors of mobility and diffusion are nonzero and can be regarded as permutations of the mobility and diffusion referring to the nonmagnetized case [58]. In such an approach, classical diffusion is considered.

Lieberman and coworkers [5,41–43] have done many efforts for developing analytical models for magnetron discharges. Wendt and Lieberman [5,42,43] developed a two-dimensional analytical model. The discharge area was split up into arch-shaped areas, with the shape determined by the magnetic field lines. In this way, the authors were able to relate the width of the sputter erosion profile to the discharge voltage and current, and the magnetic field strength, through the Larmor radius [5]. Also the light emission could be described with this model [41]. In [43], two different models for the movement of the electrons in a cylindrical postmagnetron have been proposed and compared with experimental data.

In [46–48], a particularly interesting result has been the prediction of the appearance of a negative space charge region due to the highly restricted electron mobility at strong magnetic fields and low pressures. This result has been later on validated by more realistic particle simulations for both cylindrical [36] and planar magnetrons [37]. Recently, an analytical model has also been proposed for an RF sputtering system [49].

Analytical models have also been used intensively by Bradley and coworkers. In a series of papers, they have investigated different parts of the magnetron discharge, such as the cathode fall [50], the presheath [51], and the bulk plasma [52]. All these studies are based on an earlier work by the same author [59], which is a one-dimensional fluid description. In [50,51] the classical diffusion has been replaced by Bohm diffusion and the results have indicated that the later is a more realistic mechanism for the electron transport across the magnetic force lines.

Recently, Möller [53] proposed an analytical model for a reactive magnetron plasma (argon – nitrogen gas mixture), based on a balance between ion generation and transport. Ar^+, as well as N_2^+ and N^+, ions were considered in this model, and it was assumed that all ions, created in the plasma by electron-impact ionization, arrive at the target in a free-fall transport regime. Beside the different ion fluxes, also the fluxes of reactive N atoms and N_2 molecules to the target were estimated. These data formed the input for surface processes, such as sputtering and implantation for the various ions, and adsorption for the neutral species [53].

Finally, Buyle et al. have recently developed a self-consistent two-dimensional semi-analytical model for a DC planar magnetron, to reproduce the magnetron dependence on external parameters over a wide range [54–57]. This model will be explained in more detail in Sect. 3.4 below.

A general disadvantage of analytical models is that they are unable to describe quantitatively the complex electron motion in the multidimensional electric and magnetic fields crossed at arbitrary angles, which is the situation in real sputter magnetrons, especially in the planar ones. However, analytical models have proven to be an important step in the understanding of magnetron discharges, with several advantages compared to complicated numerical simulations. Their main advantages are the relative simplicity, the ability to produce fast results, and the fact that the results are intuitively easy for understanding. They are particularly suitable in situations where the main purpose of the model is to define whether a given phenomenon is important or negligible. Such example is the electron recapture at the cathode, which has been studied by the semi-analytical model described by Buyle et al. (see also Sect. 3.4 below) [54–57]. The model has shown unambiguously the major importance of electron recapture at the cathode, and these results have later been confirmed by particle simulations [37].

3.2.2 Fluid Models

Fluid models are based on the continuity, the momentum and mean energy conservation equations of the plasma species. By coupling these equations to the Poisson equation, the electric field distribution can be calculated in a self-consistent way.

Fluid methods find extensive use, for instance, in the field of aerodynamics. However, they are not so commonly used to describe magnetron

discharges [48,59–64]. Indeed, magnetron discharges cannot be so easily considered as a fluid. The main reason is that they are operated at relatively low pressure (typically several millitorr). At such low pressure, the main assumptions of the fluid theory are not necessarily valid. An additional difficulty arises from the complicated forms of the equations of the magnetohydrodynamics, which describe a magnetized fluid. If these equations are applied to arbitrary magnetic and electric fields, they require elaborated discretization, resulting in long computation times. Another issue is the validity of the classical diffusion at high ratios of the magnetic field and the gas pressure. At relatively weak magnetic fields and relatively high gas pressure, fluid models with simplified transport coefficients can be employed. This has been done in [61], where the bulk plasma in an RF cylindrical postmagnetron has been simulated and the results have been compared to a particle simulation. A fluid description has been used also to develop a theory of the cathode sheath in magnetrons [62]. A two-dimensional fluid model using the drift-diffusion theory has been reported in [63]. It is, however, applied to conditions, which are different from typical sputtered magnetron conditions, i.e., a pressure of several torr and a magnetic field weaker than 100 G.

An attempt to overcome the complexity of the full magnetohydrodynamics equations of the electron transport [65] was recently proposed in [64]. In this paper, the presence of the magnetic field is included as a perturbation to the flux equations describing the nonmagnetized case and assuming a classical transport. However, it can be argued that the electrons are so strongly magnetized that this aspect cannot be represented in their transport by a perturbation. Hence, the condition for applying the perturbation formalism is thus violated.

3.2.3 The Boltzmann Equation

The maximum information with minimum assumptions about the discharge can be obtained by kinetic models. As mentioned above, they can be divided into two groups: either solutions of the Boltzmann equation or particle simulations.

The direct solution of the Boltzmann equation has been a popular tool for plasma modeling for many years. For magnetron discharges, the Lorentz force needs to be included. Adding the Lorentz force term, however, complicates significantly the solver and makes it impractical in two and three dimensions and for arbitrary magnetic fields. There is one situation where it can, and has been, successfully used in magnetrons. This is the simulation of cylindrical postmagnetrons, where in a large part of the discharge the magnetic field is one-dimensional and constant, which simplifies the Boltzmann equation. This is illustrated by the work of Porokhova et al. [66–73].

To find a self-consistent solution for a given input of magnetic field strength, gas pressure and discharge current, the Boltzmann equation was

supplemented by some other requirements. In [67], self-consistency was reached by adding an equation, describing the ion motion in the collisional regime (i.e., a fluid model for the ions) and the Poisson equation. In [69] the radial distribution of the electric field was determined by fixing the discharge voltage to the experimentally measured one and by demanding that the radial potential distribution provides a radial electron density distribution that is similar to the experimentally measured one. This latter approach seems "less self-consistent" because both the discharge current and voltage are used as input parameters. In [67] the model was one-dimensional, whereas in [69] the model was extended to two dimensions, so that also the axial inhomogeneities generated by the shields at the ends of the cylindrical postmagnetron can be modeled. A major advantage of the method is the small computational load: a typical calculation requires about 2–10 min, depending on the number of grid points [74].

The presented results in the above-mentioned references show a very good agreement with experimental data. However, the results were obtained at relatively high gas pressure (above 3 Pa) and relatively weak magnetic field strengths (maximum 400 G). It would be interesting to see whether this modeling approach can deal with low pressures and strong magnetic fields, as these are the working conditions where anomalous electron transport can be expected. Furthermore, it is also not evident to adapt this technique to a two-dimensional model for the planar magnetron discharge, due to the nonuniform magnetic field [74].

3.2.4 Monte Carlo Simulations

In MC simulations, computational test particles that represent a large number of real plasma particles are followed. Their movement is subject to the applied forces and the collisions of the particles are included by using probabilities and random numbers. This technique is very easy to implement and fast to compute. Its main disadvantage is that the forces must be an input, i.e., the simulation is not self-consistent.

There are many MC simulations, often called direct Monte Carlo simulations (DMCS), of different types of magnetrons reported in the literature. Among them are [75–83], which have contributed largely to the understanding of the transport and collision properties of the charged particles in magnetron discharges. The group of Sheridan–Goree et al., e.g., [75–79], was able to simulate the ionization distribution using a two-dimensional MC model and compared it with optical emission measurements. The basis of their model was a simple retracing of the high energy electron orbits by numerically integrating the Lorentz equation and combining this with a MC approach for the collision events. Similar work is reported in [84,85]. The group Sheridan–Goree also simulated the ion motion [78] and the influence of the magnetic field [79] using the same Monte Carlo model.

Ido et al. used a MC model to simulate the erosion profile in planar magnetrons. First, the erosion profile in a cylindrical and a rectangular magnetron was simulated for various pressures and magnetic field configurations [85–87]. Then, the erosion profile using ferromagnetic targets was simulated. They report how the eroded region can be influenced by placing a ferromagnetic ring on top of the target [88] and by the outer part of the yoke [89]. For a ferromagnetic target, the eroded region strongly influences the magnetic field strength. In [90] it is reported how this effect is taken into account, which leads to a very accurate erosion profile simulation.

The main advantages of the MC method are that it is easy to implement, it can handle the low gas pressures encountered in magnetron discharges, and it is much faster than self-consistent methods, such as PIC-MCC models. Therefore, it can be used on (large) three-dimensional geometries, see e.g., [91–96]. In all these references the MC model is basically used to investigate the cross corner effect. This term is used to denote the enhanced ionization and erosion that occurs at opposite sides of a (long) rectangular target, and which is attributed to a disturbed $E \times B$ drift of the electrons after they drifted through the end region of the racetrack. Here, the MC method has an advantage over the PIC-MCC method: In [97] a three-dimensional magnetron was simulated but the variation of the ionization along the racetrack was too large to notice the cross corner effect. Although the PIC-MCC method should undoubtedly be able to reproduce this effect, it would cost an enormous computational effort.

Another example illustrating the beneficial use of a MC model is the explanation of the so-called plasma emission redistribution (PER) effect [98]. This effect occurs during pulsed magnetron sputtering. When the plasma emission of a single pulse is observed, it was noticed that at the very beginning of a pulse the emission came predominantly from the turnaround regions of the racetrack, whereas in steady state, the emission came predominantly from the central straight sections of the racetrack. Using a MC model and adapting the settings for the situation at the very beginning of a single pulse, this effect could be reproduced and the origin of the effect could be retraced, as explained in [98].

Finally, the last application mentioned here for MC simulations of magnetron discharges is the simulation of the sputtered atoms transport, as was also briefly discussed in Sect. 3.1.4. These are normally non-self-consistent trajectory calculations of the sputtered particles with included collisions with the background gas atoms [23, 24, 89, 91, 99–105]. In this way the spatial distribution of the sputtered atoms and their energy and angular distribution at the substrate are calculated. This allows accurate predictions for the quality of the deposited film. Possible effects of the spatial location of the target and the substrate can be easily studied. Input is needed for the starting positions of the sputtered atoms at the cathode. This is usually taken either from an experimentally measured erosion profile or from a calculated erosion profile by a particle model.

3.2.5 Hybrid Models

While electrons are heavily magnetized, as discussed above, the ions can be considered practically nonmagnetized, due to their large masses. Therefore, in contrast to the electrons, they can be well described by a classical fluid approximation. This assumption forms the foundation of the so-called hybrid models. Hybrid models are usually a combination of fluid and particle models. In the simulations of nonmagnetized glow discharges (e.g., [106]), the ions and the bulk electrons are regarded as a fluid, while the energetic (beam-like) electrons, emitted from the cathode or generated in the sheath, are simulated as particles, i.e., fully kinetically. This approach combines the precision of the kinetic models with the relatively higher speed of the fluid codes and successfully overcomes the low pressure restrictions.

Magnetron simulations based on the hybrid model are explained in [9, 107–115]. Shidoji et al. were able to simulate the magnetron discharge and its dependence on external parameters, such as the gas pressure, the electrical power [92], and the magnetic field strength [114]. Also the influence of balancing the magnetic field [111] and of depositing an insulating layer [109] were investigated. Vyas and Kushner [31] used a modification of their two-dimensional hybrid plasma equipment model [115] to simulate a hollow cathode magnetron discharge. The effect of power and pressure was investigated, as well as the influence of magnitude and orientation of the applied magnetic fields.

The limits of validity of hybrid modeling for magnetron discharges are discussed in [112]. It is reported that the application of the hybrid model becomes problematic for strong magnetic fields and/or low gas pressures. Indeed, in such cases the results appear unrealistic: a large amount of ionization occurs at rather large distance from the cathode. The reason is that at high magnetic field strengths the electrons hardly diffuse across the magnetic field lines anymore when using the classical theory. Consequently, an electric field is formed between the sheath region and the anode. Because of this electric field, ionizations occur in that region. Also the simulation results reported in [114] express this behavior: The ionization in the region from 10 to 40 mm above the target is stronger for a magnetic field strength of 360 G than for 180 G but the peak ionization is lower. This is opposite to the behavior reported in [116]: there the simulated peak ionization rate increases with increasing magnetic field. The latter result appears more realistic, as the magnetic field is applied to the discharge to intensify the magnetron discharge, not to spread it out.

The problem of the hybrid model to deal with strong magnetic fields is probably due to the fact that it does not account for the anomalous electron transport. Indeed, as mentioned, the slow electron transport is typically treated using a fluid model. This requires the electron diffusion coefficients

for the transport perpendicular to the magnetic field lines. This coefficient is obtained using the classical theory, i.e.

$$D_{\perp} = \frac{D_{B=0}}{1 + \frac{\omega^2}{\nu^2}},$$

with $D_{\perp}$ the diffusion coefficient in the direction perpendicular to the magnetic field lines and $D_{B=0}$ the one without magnetic field. However, according to experimental evidence (e.g., [117]), the diffusion across the magnetic field lines is larger than predicted by $D_{\perp}$. This problem of uncertainties in the electron transport coefficients has been partially overcome by using the data provided by a parametric study performed by numerical solution of the Boltzmann equation for given sets of reduced electric and magnetic fields [113]. Similarly, Vyas and Kushner [31] derived the transport coefficients, for use in the fluid equations, from a kinetic simulation, to enable the fluid algorithm to represent more accurately the low pressure operation.

The second limitation of a hybrid model is the fact that the ions are not at all characterized by a Maxwellian distribution, which questions their description as a fluid. The third problem is related to the criterion of selecting which electron can be considered slow. In the nonmagnetized situation [106] the discharge is in a positive space charge mode. Hence, once the electron has traversed the sheath and has an energy below some threshold, it can be transferred to the slow group. In magnetrons, depending on the reduced magnetic field, there can be a negative space charge mode. This means that even if the electron energy is below the threshold at a given moment, the electron can still become fast. This is definitely the situation at high reduced magnetic fields. This situation has led to a modification of the classical hybrid scheme, where all the electrons are treated kinetically, while only the ions are described as a continuum [114]. In this way, the first and the third drawbacks are eliminated, but the computational cost, however, approaches that of a particle model.

In conclusion, the main advantage of the hybrid model is that it is faster than the PIC-MCC models discussed below (a solution can be obtained in 2–3 days). The payoff for this advantage is that assumptions need to be made about the slow electron motion in crossed electric and magnetic fields. Because of the latter, this technique seems to fail to describe the anomalous electron transport that occurs for strong magnetic fields and/or low gas pressures.

3.2.6 PIC-MCC Simulations

When the calculation of the electric field produced by the external power source and the spatial distribution of the plasma charged particles is added to a MC simulation, the whole simulation becomes self-consistent. It is commonly referred to as PIC-MCC simulations [118]. PIC-MCC simulations are the most powerful numerical tool for the investigation of magnetron discharges. They

can cope with the low operating pressures and the strongly inhomogeneous field and density distributions. In addition, they are capable of providing a full picture about the processes occurring in the discharge chamber. The drawback of the PIC-MCC simulations is their extensive computational load. This is especially true when two- and three-dimensional simulations are needed, especially for simulating magnetron discharges. The latter is related to the long characteristic times (typically longer than 10^{-5} s) for achieving a steady state.

Simulations of cylindrical postmagnetrons have been performed in one dimension [36,119]. Planar magnetrons can, however, not be simulated with a one-dimensional code. A full three-dimensional PIC-MCC model of a planar magnetron has been reported [97,120]. It has shown the lack of angular dependence in axisymmetrical planar magnetrons. This result has opened the way for simulating this type of magnetrons by a two-dimensional model in cylindrical coordinates. The first very thorough work of that kind has been [116] followed by [121]. The PIC-MCC method has also been successfully applied to RF sputter magnetrons [122]. Moreover, quite some work reports planar magnetron simulations using the OOPIC code [4,6–8]. This OOPIC code was developed by Verboncoeur et al. [123] and can be downloaded freely [124]. Another software package that is used for magnetron discharges is PEGASUS, which combines PIC-MCC simulations with Gaussian fitting, to investigate the erosion [125]. The software itself is described in more detail in [126,127] and is based on NEPTUNE. The latter is used in [1] to simulate copper deposition by magnetron sputtering. Furthermore, the influence of the dielectric target in an RF sputtered magnetron has been investigated in [128]. Recently, a hybrid PIC-MCC – ion relaxation model has been reported [129]. Here, the electrons are resolved in a standard PIC-MCC algorithm, whereas the ionic distribution is calculated by a continuum relaxation model.

In [4] and [6] it is reported that no steady state is found in the PIC-MCC simulations, but the number of particles was continuously increasing. In both cases, however, the time during which the plasma is simulated was very short (5 and 3 µs, respectively). Following the discharge for a longer time period apparently leads to a steady state, e.g., [8,97,116]. However, it can be argued that a reliable steady state, i.e., a steady state where the discharge evolves to the correct region of the current–voltage characteristic, can only be reached by including an external electric circuit [37]. The required time for reaching convergence is then typically about 20 µs [37], whereas the results of [8] suggest that convergence was reached after roughly 10 µs. We have developed our own PIC-MCC model for a planar magnetron discharge, which includes the external circuit [37] and accounts for the gas heating and the sputtered atom transport and collisions [38]. This model will be discussed in detail further in this chapter.

It is clear that PIC-MCC simulations produce a wealth of data. However, care has to be taken when interpreting the results. Here we mention some shortcomings of the results reported by the group of Nanbu et al. [97,116,121]. First, the time step Δt used for the electron orbits is rather large: in [116]

it is mentioned that $\Delta t \approx 0.2$ ns. The examined magnetrons have B_{max} in the range of 325–650 G. With these B_{max} correspond Larmor frequencies of 6–11 GHz, which means that Δt varies from 0.18 to 0.36 times the inverse of the Larmor frequency. In [130] it is argued that such large time steps result in an inaccurate orbit calculation and in a serious artificial electron energy loss. These inaccuracies compromise both the position and the amount of ionization simulated, which seriously questions the reliability of the presented results. This might be the origin of the second shortcoming of these simulations: the simulated cathode sheath thicknesses are very large, in [116] sheath thicknesses vary from 4.5 to 5.8 mm. In reality, a sheath thickness of at most 3 mm is observed (e.g., [91, 130, 131]). Third, the current densities are extremely low for magnetron discharges. From the sketch of the magnetron configuration in [116] we can infer a racetrack surface of roughly 24 cm^2 (racetrack length $\approx$24 cm and width $\approx$1 cm). The total currents listed in the article are between 35 and 50 mA, which means current densities around 1.5–2.1 mA cm^{-2}. These values are at least a factor 10 lower than the current densities typically encountered in magnetron sputtering. This discrepancy can again be attributed to the necessity of including an external electric circuit [37]. The fourth remark concerns the simulated current–voltage characteristics: With increasing discharge voltage the discharge current and the electron density are found to decrease, the cathode sheath thickness is found to increase [121]. These simulated dependences are opposite to experimental observations (e.g., [130, 132]).

On the other hand, a very interesting result of the PIC-MCC simulations is the magnetic field dependence: in [116] the magnetic field strength B_{max} is varied from 325 to 650 G at constant discharge voltage (V_d = 500 V) and gas pressure (0.67 Pa). The simulations show an increase in the plasma density and in the ionization rate. Moreover, the discharge intensifies and the cathode sheath thickness is found to decrease. This is in agreement with common sense: with increasing magnetic field strength, the magnetron intensifies and is better confined. This result seems to indicate that the anomalous electron transport is, at least qualitatively, correctly simulated (see also the discussion about the hybrid model above).

In spite of the mentioned shortcomings, the PIC-MCC technique is in principle a very viable method. Hence, we may conclude that PIC-MCC simulations are the most powerful tool to tackle the problem with the full description of the planar magnetrons at all operational conditions. The price for that, however, is the very long computation time.

3.3 Challenges Related to Magnetron Modeling

No matter how sophisticated a simulation model is, there are some limitations to what can be expected from the calculation results. The origin of this might be due to inadequate experimental input data or to the specific geometry or

operating conditions of the process. As such, these situations can be called problem cases or, more positive, challenges related to magnetron modeling. Here, we give a list of the most important ones of these challenges.

3.3.1 Secondary Electron Emission Yield (γ)

The secondary electron emission yield γ denotes the number of secondary electrons emitted per incoming ion. The magnetron characteristics depend very strongly on the exact value of the secondary electron emission yield. Unfortunately, these yields are extremely difficult to measure. Consequently, for most materials this yield is not accurately known.

This is probably the most fundamental factor limiting the output of magnetron simulations: whatever model used for the magnetron simulation, it can only give accurate results when the applied secondary electron emission yield is correct. In Shidoji et al. it is mentioned that reducing the secondary electron emission yield by 50% can decrease the currents with a factor four to five [9]. In [116] an increase of the secondary electron emission yield from 0.12 to 0.15 leads to a substantial increase in the plasma density (from 1.1 to $1.7 \times 10^{10}\,\mathrm{cm}^{-3}$) and in the discharge current (from 34.9 to 49.5 mA).

Given this situation, the values for the secondary electron emission yield used in magnetron simulations strongly vary. Usually, γ is taken to be independent of the discharge voltage (e.g., in [97,120]). On the other hand, Shidoji et al. use a secondary electron emission yield that depends on the discharge voltage [9]. Sometimes, quite unrealistic values for the secondary electron emission yield are used, e.g., in [133] where for certain conditions a secondary electron emission yield of 5 is assumed for a metal surface. Also in [125] γ is used as a tuning parameter: the authors mention that it is set to 0.03 as *a larger value sometimes leads to the unbounded increase of superparticles*, i.e., the simulation does not reach a steady state but the plasma density continues to increase.

The challenge here is to make the magnetron simulations so reliable that, once the model is calibrated using a material with a relatively well-known secondary electron emission yield, comparison of the experimental and simulation results can be used to determine the secondary electron emission yield of the investigated target material. This is, however, a very ambitious goal, due to the many other uncertainties in the models. Therefore, efforts should also be made for accurate measurements of the secondary electron emission yield. In this respect, Depla et al. recently determined ion induced secondary electron emission yields for several oxides [134].

3.3.2 Recapture

The orbit of a secondary electron emitted from the target follows the magnetic field lines. When the electron does not interact with the discharge gas, this will lead to an electron–target interaction. This event is characterized by

the reflection coefficient R, which gives the probability that the electron is reflected. If the electron is not reflected, it is recaptured by the target (see also Sect. 3.4 below).

To simulate this effect accurately, the initial electron energy may not be neglected, the orbit calculation should be performed very accurately and the reflection coefficient R needs to be known. The required accuracy has important consequences as it can only be reached by reducing the time step used for retracing the electron orbits, which seriously increases the computational effort. In [130] it is shown that the time step needs to be at least a factor of two smaller than currently encountered in magnetron simulations. Second, experimental values of R, needed as input for the simulation, are very scarce. This is highly inconvenient because the process of recapture is quite sensitive to this reflection coefficient [37, 135].

3.3.3 Electron Mobility

The problem of the anomalous electron transport was already mentioned above in Sect. 3.2.5. Indeed, the electron transport in the direction perpendicular to the magnetic field lines is larger than expected from classical diffusion theory. The enhanced mobility is probably due to oscillations in the electric field.

This effect has its consequences for magnetron modeling. Obviously, all methods that rely on the classical theory are affected. This is especially true for the models that rely on the fluid theory, as this requires diffusion coefficients (see also the discussion about the hybrid model in Sect. 3.2.5).

In principle, the PIC-MCC method should be able to deal with this problem as it uses no assumptions about the particles. However, a culprit here might be the timescale at which the phenomena occur. A broad range of oscillation frequencies have been observed in plasmas, but the typical frequency range is of the order of some 100 kHz, corresponding with a period of 10 µs. Logically, it can be assumed that the discharge only reaches a steady regime after some oscillation periods. This means that the discharge should be followed during a time span of at least 50 µs. Usually, PIC-MCC simulations are not performed for such a long time, implying that they will not accurately describe the effect.

A possible way to model the enhanced electron mobility is by adding an extra type of collisions, the so-called Bohm diffusion collisions. The contribution of Bohm diffusion can then be tuned until the simulations correspond with the experimental measurements. This will be briefly explained for the analytical model in Sect. 3.4. For the modeling of Hall thrusters, a similar technique has been used, see e.g., [135, 136].

3.3.4 Modeling "Industrially Relevant" Magnetron Discharges

Of course, the magnetron discharges used for industrial sputter deposition purposes are not fundamentally different from the ones used in laboratories.

Nevertheless, there are some aspects that make them extremely challenging to simulate. In principle, including these characteristic features in the models is not a fundamental problem, but it will make the simulations much more computational intensive. Given that the computational load is already high (order of several days for both the PIC-MCC and hybrid models), it is clear that an industrially relevant virtual sputter magnetron is not for the immediate future, even taking into account Moore's law, which states that the computation power doubles, on average, every 18 months. In the following, a few of these challenges will be outlined.

Geometry

Although it is not a fundamental limit, the geometry of the magnetron considered can make certain models useless. In the glass coating industry, magnetrons with cathodes up to 4 m long are used. For such dimensions, the PIC-MCC technique becomes useless because of the unrealistically high computational effort. Hence, less computational intensive methods are needed. An example is the simulation of the effect of the turnaround region on the uniformity. For this type of simulations the MC method is currently used (see Sect. 3.2.4 above). Although the latter model has the disadvantage that the influence of the anode cannot be modeled self-consistently, it is still the preferred method for such large-scale magnetrons, as the computational load of the PIC-MCC would be forbiddingly high.

(High Power) Pulsed Sputtering

For industrial applications, pulsed sputtering is frequently used. The typical frequency range is in the order of 10–100 kHz. To simulate such processes, the magnetron needs to be followed for several periods, i.e., several times $100 - 10\,\mu s$. At this moment, this cannot be achieved by PIC-MCC modeling. A good candidate for this type of problems would be a hybrid model.

Currently, high power pulsed sputtering is gaining interest because of its potential to deposit coatings with unique properties. In such discharges extremely high electrical powers are applied during short intervals. Because of the high plasma density, typical approximations made in magnetron modeling are not valid anymore. First, the magnetic field strength in the magnetic trap region changes because of the large Hall currents induced during the high power on-pulse [137]. In all simulation models known to us, this influence is not accounted for.

Second, because of the high ionization degree in these high power discharges, it will not be possible anymore to neglect the interactions between charged particles (Coulomb collisions). Again, most simulation models for planar magnetrons neglect this type of interactions. In [138] a cylindrical postmagnetron is simulated with a PIC-MCC model, taking into account electron–electron interactions, albeit in a simplified way. We have included

these interactions in our PIC-MCC model [38, 39], based on the method described by Nanbu [139–141].

Third, the gas density reduction or gas rarefaction: in Sect. 3.6, it is discussed how the energetic plasma particles can heat the discharge gas, which leads to a gas density reduction. For standard operating conditions, this effect can be neglected. However, in high power pulsed sputtering this will not be the case. This effect is usually not accounted for in magnetron models. To our knowledge, only the PIC-MCC model described in this chapter (Sect. 3.6) is able to deal with this effect [38, 39].

Accuracy

The specifications for sputter-deposited coatings can be very strict. A typical example is the required coating uniformity. Even for large area coating of glass (with cathode lengths of almost 4 m) the required uniformity is usually better than $\pm 0.2\%$. It is not evident for a numerical technique to reach this level of accuracy. For an MC technique, the only way to reach this is by following a sufficiently large number of particles, i.e., the accuracy comes at the cost of computational load.

Apart from this, several other effects influence the accuracy at this scale. Some examples are the gas heating due to sputtered particles and the resulting gas density reduction, a nonuniform gas inlet, the influence of the erosion groove formation on the process, redeposition on the target, heating of the target, the influence of the sputtered particles, etc. Again, all of these examples form no fundamental problem, but they might seriously increase the computational effort.

Basically, the mentioned effects are all examples of "extended self-consistency." Usually, in magnetron modeling the term self-consistency is used with respect to the electric field. However, because of the on-going sputtering and deposition during the process, the environment of the magnetron changes. For a very accurate magnetron simulation, also these changes have to be taken self-consistently into account.

3.4 Two-Dimensional Semi-Analytical Model for a DC Planar Magnetron Discharge

In this section, the self-consistent two-dimensional semi-analytical model developed by Buyle et al. for a DC planar magnetron [54–57, 130] will be explained in more detail, because it is very powerful, in spite of its simplicity. Also some characteristic results will be presented.

3.4.1 Description of the Model

Ionization Model

First of all, an ionization model was developed, to calculate the ionization rate due to the high energy electrons, i.e., defined as the electrons with energy above the threshold for ionization. For this purpose, the discharge area was split into arch-shaped regions. This can be justified, because the collisionless motion of these high energy electrons is limited to such arch-shaped regions. The effect of electron collisions with the background gas was analytically modeled as a probability for the electrons to hop from one arch to another.

Output of this model was the spatial distribution of ions, generated by a single electron emitted from the target. It was found that the ionization distribution is not directly influenced by the gas pressure. This characteristic could be used by future models for magnetron discharges, to reduce the computational load.

Another important result was that a substantial amount of ionization occurs in the cathode sheath of the magnetron. This so-called sheath ionization is important because the electrons generated in this way can be further accelerated and give rise to more ionization. This effect was characterized by a multiplication factor, which is defined as the ratio between the total number of ions generated due to the emission of a single electron, and the theoretical number of ions that can be generated without sheath ionization. The multiplication factor was found to be close to one for electrons emitted at the edge of the racetrack, but it can rise to values of 3–5 for electrons emitted close to the racetrack center. Therefore, an average multiplication factor, $\langle m \rangle$, was introduced.

Effect of Electron Recapture

Furthermore, the process of electron recapture at the cathode was taken into account by introducing the effective gas interaction probability (EGIP), defined as:

$$\mathrm{EGIP} = f = 1 - \exp\left(-\frac{s}{l}\right), \tag{3.1}$$

where s is the average distance traveled by the electron before it is recaptured at the cathode and λ is the mean free path length of the electron. For typical magnetron operating conditions (300 V discharge voltage, 600 G maximum magnetic field strength, and 0.5 Pa gas pressure) the EGIP was typically found to be around 1/3, i.e., about 2/3 of the electrons appears to be captured.

Self-Consistent Model

The model was made self-consistent by considering the ionization distribution from a large number of electrons emitted from the cathode, taking into

account the multiplication factor and EGIP for each electron. Indeed, from the ionization distribution, obtained in this way, the ion bombardment at the target can easily be deduced. This determines the average number of emitted electrons, based on the ion-induced secondary electron emission yield (γ). In this way, the model is made self-consistent, by iterating through this process, and demanding that the original and the new secondary electron emission profiles should be identical.

With this model, the Thornton relation [142] for determining the minimum discharge voltage at which the magnetron can be maintained is extended to a general relation:

$$V_{\mathrm{d}} = \frac{W}{\gamma < fm > \varepsilon_{\mathrm{e}}\varepsilon_{\mathrm{i}}}, \tag{3.2}$$

where W is the effective ionization energy ($\sim$30 eV for argon), ε_{i} is the ion collection efficiency, and ε_{e} stands for the theoretical number of ions that the electron efficiently generates before it is lost from the discharge. Both ε_{i} and ε_{e} can be assumed equal to one for typical magnetron conditions.

Note that in the original Thornton relation, sheath ionization is not considered ($m = 1$) and the EGIP (f) was assumed equal to 0.5. Because the model developed by Buyle et al. is two dimensional and includes the magnetron configuration (geometry and magnetic field strength), f and m can be calculated more accurately. This extended Thornton relation illustrates that the pressure and magnetic field influence the magnetron discharge through f and m, as all the other quantities in the formula are constant for a given target material and typical magnetron conditions.

Calculation of the Discharge Current

Furthermore, to deduce the discharge current (I_{d}) from the obtained magnetron properties, the line current density, j_{m}, was introduced, which is related through the racetrack length, L_{rt} as: $I_{\mathrm{d}} = j_{\mathrm{m}} L_{\mathrm{rt}}$. To determine j_{m}, the Child-Langmuir law had to be extended, leading to the following relation for j_{m}:

$$j_{\mathrm{m}} = j_{\mathrm{d}} A_{||,\mathrm{t}} A_{||,\mathrm{s}} \int B(x)\mathrm{d}x, \tag{3.3}$$

where j_{d} is the surface current density, the factors $A_{\|,\mathrm{t}}$ and $\mathrm{A}_{\|,\mathrm{s}}$ account for the fraction of ions generated within the sheath (typically between 1/4 and 1/2), and for the ions that are generated scattered over the racetrack length, respectively. Finally, the integration is needed to convert the surface current density, j_{d}, into the line current density, j_{m}, and accounts for the nonuniformity across the racetrack (x is the direction across the width of the racetrack).

Using this relation, the discharge current could be calculated. The model was able to reproduce the behavior of the magnetron discharge with decreasing pressure and constant current. Also typical current–voltage characteristics

could be simulated. However, it appeared that the extreme steepness of the current–voltage characteristics was missing, and that the influence of the magnetic field on the gas pressure dependence was not retrieved. This example clearly illustrates the possibilities and limitations of analytical modeling.

Effect of Coulomb Collisions and Anomalous (or Bohm) Transport

Finally, to resolve the discrepancy between the simulated and experimental results, two processes not included in the model so far were examined, i.e., Coulomb collisions and Bohm (or anomalous) diffusion. The first process could explain the magnetic field dependence of the pressure effect in cylindrical (or post) magnetron discharges, but it can be ruled out for planar magnetrons, because the high energy electrons are too energetic.

The latter process was added to the model in an empirical way, by introducing an artificial type of interactions, the Bohm diffusion collisions. The idea comes from Hall thruster simulations, where a similar approach is followed [135, 136]. The Bohm diffusion collisions represent the electron interactions with the electric field oscillations, which are supposed to generate anomalous diffusion. The "amount" of Bohm diffusion is defined as the occurrence of the Bohm diffusion collisions relative to the standard collisions (ionization, excitation, and elastic collisions), and it is proportional to the magnetic field and inversely proportional to the gas pressure, indicating that anomalous electron transport is especially important at strong magnetic fields and low pressures.

The influence of increasing the "amount" of Bohm diffusion on the magnetron properties was simulated. These changes could be related to the increased electron mobility in the direction perpendicular to the magnetic field lines. The main advantage of including Bohm diffusion is that it enables to reproduce the extremely steep current–voltage relations, which are characteristic for a magnetron discharge.

3.4.2 Examples of Calculation Results

The results of this analytical model were compared with experimental results, using two input values, i.e., the electron reflection coefficient and the relative occurrence of Bohm diffusion collisions, as tuning parameters. Two examples will be discussed in the sections below. In both cases the experimental results were obtained using a commercially available planar circular magnetron (Von Ardenne PPS50, see also Sect. 3.5).

Calculated Ionization Distribution vs. Measured Plasma Emission Distribution

Figure 3.2 shows the plasma emission recorded as a function of distance perpendicular to the target. The experiment and, hence, the results are very

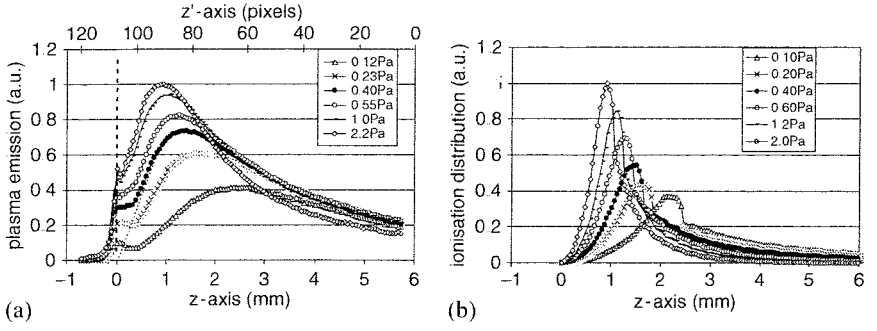

Fig. 3.2. The influence of the gas pressure on the optical emission of the magnetron at 50 W, as measured (**a**) and as simulated (**b**). Note that the emission has been normalized to the maximum emission at 2.2 Pa (2.0 Pa) for the experiments (simulations). The *dashed vertical line* (part **a**) indicates the position of the target. The *dotted line* (part **a**) suggests the "true" emission, i.e., without target reflection, for the case of 0.40 Pa.

similar to what was measured by Lan Gu and Lieberman [41]. The z'-axis represents the distance along the direction perpendicular to the target (expressed in pixels). The vertical line at $z' = 107$ indicates the position of a small peak that is due to the light that reaches the camera after reflection on the target. According to [41] the exact position of the target surface is probably at slightly lower z'-values. The z'-axis in pixel-scale could be converted into the z-axis in mm-scale.

In the analytical model the light emission of the plasma is not simulated. However, the excitations and ionizations generated by the high energy electrons occur practically at the same positions. Hence, the ionization rate distribution can be used for comparison with the experimentally measured emission intensity and is plotted in Fig. 3.2b. As one can see, the shift of the peak and the decreased intensity with decreasing pressure are reproduced very well.

Current–Voltage Characteristics

For a second example of the analytical model, the discharge voltage is calculated as a function of the electrical current for different secondary electron emission yields (γ) at constant pressure (0.3 Pa). The variation in γ was experimentally achieved by using different target materials under otherwise identical experimental conditions. Figure 3.3 shows that the increasing steepness of the current–voltage characteristic with increasing γ is reproduced nicely. The relative spacing between the curves is also reproduced very well for $\gamma = 0.06$ through 0.14. For $\gamma = 0.18$ the experimental curve lies much closer to $\gamma = 0.14$ than the simulated one. A possible explanation might be that the choice of yttrium (Y) as material for obtaining the experimental curve corresponding

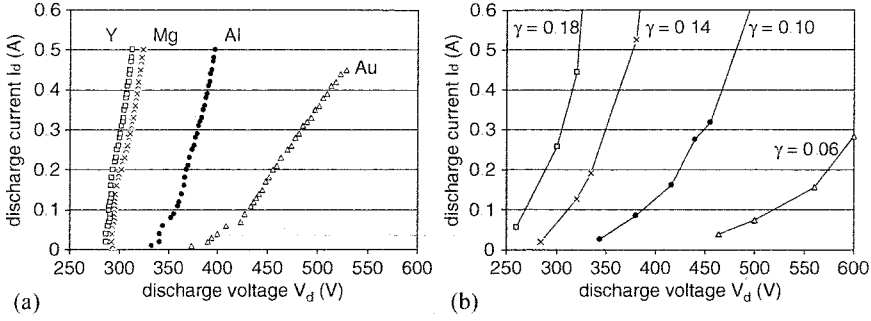

Fig. 3.3. Influence of the secondary electron emission yield γ on the current–voltage characteristics at 0.3 Pa, as measured (**a**) and as simulated (**b**). The experimental curves are obtained with different target materials: Au, Al, Mg, and Y. The corresponding γ-values used in the simulation for these materials are 0.06, 0.10, 0.14, and 0.18, respectively, as described in [143]

with $\gamma = 0.18$, is based on a calculated value of γ and not on experimental data, see [143].

In view of the relative simplicity of this analytical model, and the fact that certain aspects are completely neglected (such as the effect of bulk electrons), the agreement between the simulations and experimental data is very satisfactory.

Therefore, it can be concluded that this analytical model is able to reproduce self-consistently the influence of the main three external parameters (i.e., magnetic field strength, gas pressure, and electrical power) over a wide range. Also the effect of the secondary electron emission yield, γ, could be correctly simulated. This indicates that the model captures the most important processes occurring in the magnetron discharge, and is therefore a valuable "virtual" tool to gain insight in the generic magnetron behavior.

3.5 PIC-MCC Model for a DC Planar Magnetron Discharge

This section will give a detailed description of the PIC-MCC model developed by Kolev and Bogaerts for a DC planar magnetron [37–39, 144]. Some characteristic results will also be illustrated.

3.5.1 Particle-In-Cell Model

The PIC model is a numerical model describing an ensemble of collisionless charged particles, which can be, but not necessarily, under the influence of an external electromagnetic force. The constituents of the ensemble are not real physical subjects. They are artificial objects, representing the main physical

properties of the real particles, such as charge, mass, and momentum. These computational particles are referred to as *superparticles* (SPs). Each SP represents a large number of real particles. This number is called *weight* and is in the order 10^6–10^9. Thus, the first approximation of PIC is the replacement of the real particles in a physical system with artificial superparticles. The second approximation is the discretization of time. This means that the simulated system jumps from one temporary state to another, in contrast to the real system, where the time evolution is continuous. The third approximation is the space discretization. Indeed, a mathematical spatial grid is imposed. The electrostatic field that results from the position of all simulated particles at a given moment of time is calculated on the grid only. The external (electric and magnetic) field, if any, is calculated on the same grid. The particles advance is then made by interpolating the forces resulting from these fields from the grid to the particle locations.

The trajectory of the SPs is simulated during a large number of time steps. A schematic diagram of a PIC *computational cycle*, over a time period Δt equal to the discretization pace in time, for the case of an external magnetic field, B and electrostatic field E, is presented in Fig. 3.4.

Before the first execution of the cycle, the initial state of the system needs to be specified. This includes the initial distributions of the particles in the coordinate and the velocity spaces. In fact, this is the main guess in a PIC simulation, so it must be a physical one. In following sections, the different steps of the computational cycle will be explained in detail.

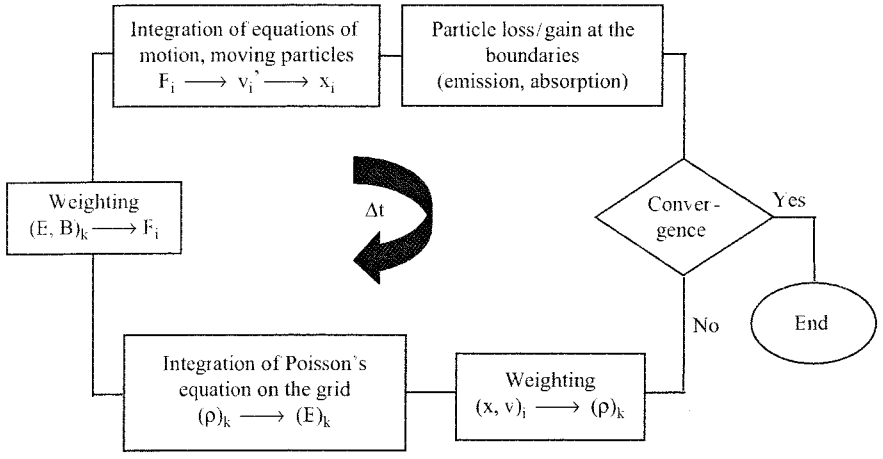

Fig. 3.4. A scheme of a PIC cycle for the case of electrostatic field, E, and an external magnetic field, B. Here v represent the velocity of the SPs, x their coordinate, F the force acting upon them, and ρ is the charge density. The index k refers to the grid and the index i to the SPs. The time step of the cycle is Δt

Integration of the Equation of Motion

In a DC magnetron, the force acting on a charged particle has two components: electric and magnetic. The gravitational force is ignored because its magnitude is very low in comparison to the electric and magnetic forces, due to the small masses of the electrons and ions. Further, the magnetic force can be considered external, because the magnetic field that results from the motion of the charges inside the magnetron is only a small perturbation to the magnetic field created by the magnets. The electric force, on the other hand, is a combination of the applied (external) electric field and the electric field induced by the charged particles. Thus the force is given by:

$$\boldsymbol{F} = \boldsymbol{F}_{\text{electric}} + \boldsymbol{F}_{\text{magnetic}} = q\boldsymbol{E} + q(\boldsymbol{v} \times \boldsymbol{B}), \tag{3.4}$$

leading to the equations of motion

$$\begin{aligned} m\frac{d\boldsymbol{v}}{dt} &= q(\boldsymbol{E} + \boldsymbol{v} \times \boldsymbol{B}) \\ \frac{d\boldsymbol{x}}{dt} &= \boldsymbol{v} \end{aligned}$$

where x denotes the coordinate. This is a system of ordinary differential equations. It is discretized by the method of finite differences [145] using central differences for maximum stability and accuracy at low computational cost. A standard way to achieve this is to use the *leapfrog algorithm*, which is explained in Fig. 3.5.

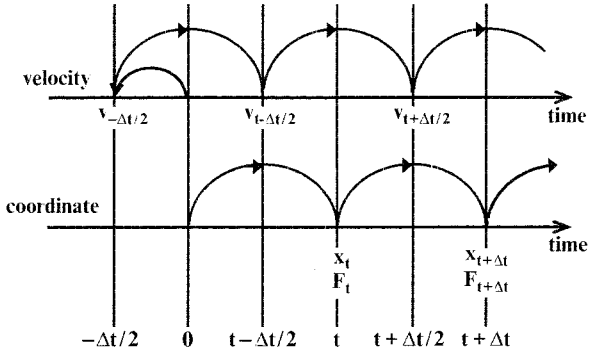

Fig. 3.5. A sketch of the leapfrog algorithm. The position of a particle is advanced from a moment t to a moment $t + \Delta t$, even though the velocity is not known in neither of the two moments, but in between. This represents the time centering. In time $t = 0$, the initial conditions are specified at the same time. That is why the velocity is initially returned half a time step back in time

The time centering is clearly seen. The application of the leapfrog algorithm leads to the following system of finite difference equations

$$\begin{aligned} \frac{\boldsymbol{v}_{t+\Delta t/2} - \boldsymbol{v}_{t-\Delta t/2}}{\Delta t} &= \frac{q}{m}\left[\boldsymbol{E}_t + \frac{\boldsymbol{v}_{t+\Delta t/2} - \boldsymbol{v}_{t-\Delta t/2}}{\Delta t} \times \boldsymbol{B}\right] \\ \frac{\boldsymbol{x}_{t+\Delta t} - \boldsymbol{x}_t}{\Delta t} &= \boldsymbol{v}_{t+\Delta t/2} \end{aligned} \tag{3.5}$$

The magnetic field is not indexed, because it is constant with time. The system (3.5) is in vector form. When written in components, it produces in general six scalar equations. Those of them that originate from the first equation are heavily coupled because of the rotation term. This makes the direct solution very complicated and computationally ineffective, because a solution is needed for every particle per each time step. The problem can be surmounted by noticing that the first term in the right-hand side of (3.5) is acceleration along the electric field and changes the magnitude of the velocity, while the second term is a rotation of the velocity vector, which does not alter the velocity magnitude. Then the force can be split into pure acceleration and pure rotation. To stick with the time centering, the acceleration can be performed in two stages, each with the half of the time step, while the rotation is performed at once, in between the two half-accelerations. In terms of velocities this can be expressed as

$$\boldsymbol{v}_{t-\Delta t/2} \xrightarrow[\Delta t/2]{half\ acceleration} v' \xrightarrow[\Delta t]{full\ rotation} v'' \xrightarrow[\Delta t/2]{half\ acceleration} \boldsymbol{v}_{t+\Delta t/2},$$

where $\boldsymbol{v}'$ and $\boldsymbol{v}''$ are some dummy velocities. Half-accelerations are trivial for handling since there is no coupling there. The rotation can be handled geometrically, as first suggested by Boris [146] and explained in detail in [144].

Charge Assignment

Once the particles' positions are calculated, the charge density, ρ, at the grid must be obtained. This procedure is called *charge assignment*. It is done, by ascribing fractions of each point charge to the neighboring grid points. To account for the charge conservation, the sum of all fractions must be equal to the point charge. The resulting charge, assigned to a given grid point is the sum of all fractions assigned to that grid point. The charge density then is the grid charge divided by some specified volume around it.

The function, which determines what fraction of the point charge is assigned to a given grid point, is called *weighting function* or *shape factor, S*. The latter term arises from the way the grid sees the particles. There are different ways to construct the weighting function. The choice is always a compromise between more accurate physics incorporated and higher computational costs.

The simplest scheme for charge assignment is the so-called nearest grid point (NGP) scheme. The NGP scheme assigns the whole point charge to the

NGP. It is computationally very attractive, but is seldom used, because of its coarseness that can introduce fatal numerical instabilities. The NGP scheme is of zeroth order.

The first-order scheme is the so-called *cloud-in-cell* (CIS) scheme, first introduced by Birdsall and Fuss [147] for one-dimensional plasma simulations. The CIS scheme uses linear interpolation to assign the charge to the NGPs. It is much more accurate and also smoother than the NGP scheme.

When still more smoothness or accuracy is desired, higher order schemes can be used. Then a point charge is assigned not only to the closest grid points, but also to one or several distant grid points. The interpolation function is then of second or higher order. The fact that it is not linear anymore leads to often unacceptable computational intensification. That is why the CIS scheme is the most commonly used scheme.

In two dimensions, the linear weighting may be performed in two ways. The first one is the complete analogue of the CIS scheme. The second one is area weighting, also known as *bilinear weighting*. When axisymmetric systems are modeled, the usual choice of coordinate system is cylindrical (r–z). Although formally two-dimensional, it in fact describes a volume. To represent this correctly in the charge assignment, the weighting is to be volumetric (r^2, z), rather than area weighting. The way it is done is shown and explained in Fig. 3.6.

Integration of Poisson's Equation on the Grid

The charge distribution, characterized by the charge density, ρ, creates an electrical potential, V, given by Poisson's equation, which in cylindrical (r, z) coordinates reads

$$\frac{1}{r}\frac{\partial}{\partial r}r\frac{\partial V(r,z)}{dr} + \frac{\partial}{\partial z}\frac{\partial V(r,z)}{\partial z} = -\frac{\rho(r,z)}{\varepsilon_0}$$

$$\rho(r,z) = q(n_i(r,z) - n_e(r,z)) \tag{3.6}$$

where n_i and n_e represent the ion and electron number density, respectively.

The discretized form of (3.6) is obtained by applying the Gauss' law, for the dashed volume, centered on a grid node (r_i, z_j) (see Fig. 3.7):

$$\frac{q_{i,j}}{\varepsilon_0} = 2\pi r_{i+1/2}\Delta z E_{r\,i+1/2,j} - 2\pi r_{i-1/2}\Delta z E_{r\,i-1/2,j}$$
$$+ \pi\left(r_{i+1/2}^2 - r_{i-1/2}^2\right)(E_{zi,j+1/2} - E_{zj,i-1/2}),$$

where the geometric factors are defined as follows

$$\Delta r_{i+1/2} \equiv r_{i+1} - r_i$$
$$\left(\Delta r^2\right)_i \equiv r_{i+1/2}^2 - r_{i-1/2}^2$$
$$\left(\Delta r^2\right)_0 \equiv r_{1/2}^2.$$

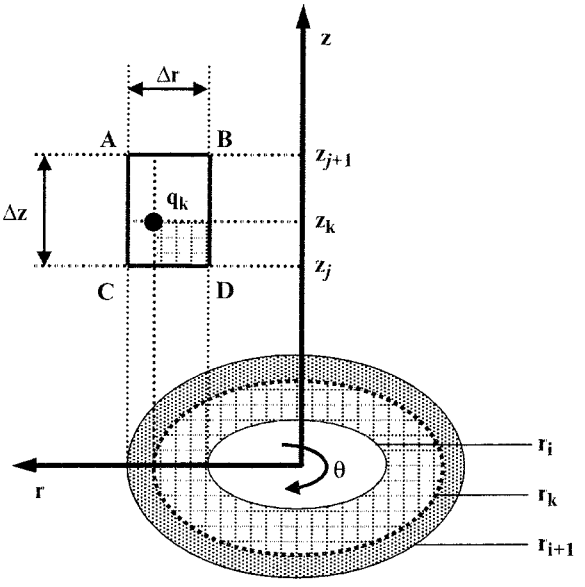

Fig. 3.6. Illustration of the charge assignment in cylindrical (r, z) coordinates, according to the volumetric weighting CIS scheme. The charge q_k, located at point (r_k, z_k), is distributed among the four grid nodes A, B, C, and D of the grid cell it is located in. The fraction of q_k that is assigned to A, for example, is equal to the product of q_k and the ratio of the volumes: (1) obtained by full rotation of the *shaded* area of the grid cell ABCD around the z-axis and (2) obtained by full rotation of the whole grid cell ABCD around the z-axis. Δr and Δz are the grid sizes in r- and z-direction, respectively

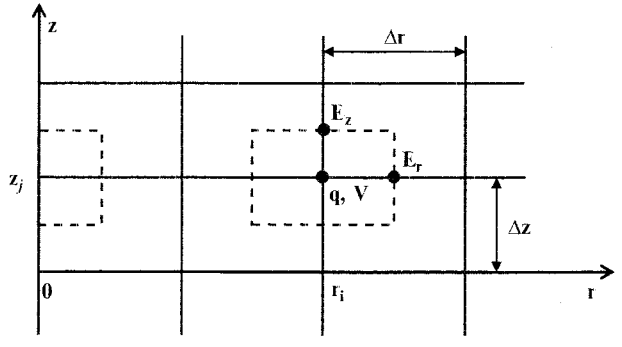

Fig. 3.7. A sketch of the computational grid with grid separations Δr and Δz. The *dashed line* centered on the grid point (r_i, z_j) represents the surface on which the Gauss' theorem is applied. The discrete values of the charge, q, and the potential, V, are known in the grid nodes, whereas the components of the electric field, E_r and E_z, are defined on the Gauss' surface. The surfaces allocated at the origin, $r = 0$, (*left-dashed box*) are half the size of those located in the volume

Employing single cell finite differencing

$$E_{r\,i+1/2,j} = \frac{V_{i+1,j} - V_{i,j}}{\Delta r_{j+1/2}} \quad E_{z\,i,j+1/2} = \frac{V_{i,j+1} - V_{i,j}}{\Delta z}$$

and using a standard five-point stencil [146], the discretized form of (3.6) becomes

$$\begin{aligned} &\frac{2r_{i+1/2}}{(\Delta r^2)_i\,\Delta r_{i+1/2}}\,(V_{i+1,j} - V_{i,j}) - \frac{2r_{i-1/2}}{(\Delta r^2)_i\,\Delta r_{i-1/2}}\,(V_{i,j} - V_{i-1,j}) \\ &\qquad + \frac{1}{\Delta z^2}\,(V_{i,j+1} - 2V_{i,j} + V_{i,j-1}) = \frac{1}{\varepsilon_0}\rho_{i,j} \quad i > 0 \\ &\frac{2r_{1/2}}{(\Delta r^2)_0\,\Delta r_{1/2}}\,(V_{1,j} - V_{0,j}) + \frac{1}{\Delta z^2}\,(V_{0,j+1} - 2V_{0,j} + V_{0,j-1}) = \frac{1}{\varepsilon_0}\rho_{0,j} \quad i = 0 \end{aligned} \tag{3.7}$$

The charge density $\rho_{i,j}$ is obtained from $\rho_{i,j} = q_{i,j}/vol_{i,j}$, where

$$vol_{i,j} \equiv \pi(\Delta r^2)_i \Delta z. \tag{3.8}$$

In the second of (3.7), an implicit boundary condition is implied representing the symmetry around the axis $r = 0$

$$\left.\frac{\partial V}{\partial r}\right|_{r=0} = 0.$$

The other boundary conditions are discussed in the next section.

Equation (3.6) is an elliptic partial differential equation with separable coefficients. This favors the use of some of the so-called rapid elliptic solvers [148], which are much more efficient than the more frequently used mesh-relaxation methods (MRM's) [149]. Since there is no periodicity in either of the directions, *fast Fourier transform techniques* [150] are inapplicable. Instead, the *cyclic reduction method* (CRM) can be employed. The CRM is more complicated from programmer's viewpoint, but it is the most efficient numerical method for the case of interest. The description of the general CRM and a possible algorithm for its implementation is given in [151]. If an equidistant grid in the z-direction is used, the CRM algorithm is even faster. An additional advantage of the CRM is that as a direct method, it is presumably more accurate than any of the MRM's, which are iterative.

External Circuit

In modeling of magnetron discharges, an external circuit needs to be incorporated, to ensure that the model describes the magnetron discharge in the correct current–voltage regime [37,144]. Figure 3.8 gives a schematic diagram of a simple external circuit, consisting of a constant voltage source, V_{ext}, and

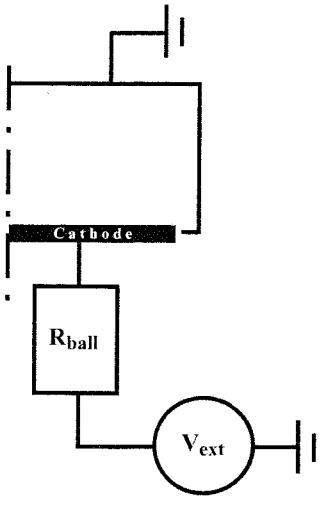

Fig. 3.8. An external circuit consisting of a constant voltage source, V_{ext}, and a ballast resistor, R_{ball}, in series with the cathode. The *dot-dashed line* represents the symmetry axis, $r = 0$

a ballast resistor, R_{ball} in series with the cathode, together with a sketch of the planar magnetron considered in the present study.

The presence of an external circuit leads to the necessity of simultaneous advance in time of the circuit and the discharge. This problem is known as *modeling of bounded plasmas with external circuits* [152]. Its numerical application in 1D has been given in detail in [152–154]. A comprehensive procedure for the case of 2D Cartesian coordinates can be found in [155]. For 2D cylindrical (r, z) coordinates, certain modifications in the procedure of [155] are necessary. This is explained in detail in [144]. In the following, a brief description is presented.

The coupling between the circuit and the discharge is maintained through satisfying the charge conservation at the cathode

$$A\frac{d\sigma}{dt} = I_{ext}\,(t) + Q_{disch} \tag{3.9}$$

where σ is the total surface charge density at the cathode, I_{ext} is the external circuit current, A is the cathode surface, and Q_{disch} is the charge deposited from the discharge on the cathode during a period dt, due to the bombarding fluxes of the charged plasma species.

The total surface charge can be determined independently of (3.9) applying the Gauss's theorem on a number of boxes, closely surrounding the cathode. This is done in the following manner. The cathode surface is divided into nr_1 boxes, as shown in Fig. 3.9.

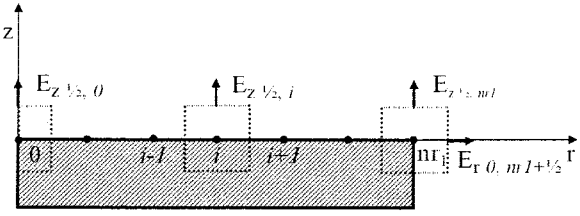

Fig. 3.9. The cathode surface ($z = 0, r \in [0;\ r_{nr1}]$) is enclosed by nr_1 boxes. For each of them, the Gauss' law is applied. For all boxes, except the one centered on $r = nr_1$, the flux of the electric field through the boxes' surfaces is nonzero only in $+z$-direction. For the box centered on $r = r_{nr1}$, there is also a nonzero flux in r-direction

For the ith box the Gauss' law is

$$\oint_{S_i} \varepsilon_0 \boldsymbol{E} \cdot \boldsymbol{ds} = Q_i,$$

where S_i is the surface of the ith box, ds is the surface element, and Q_i is the total charge inside the box. The total charge, Q_i, is a sum of the surface charge, caused by the charging of the cathode by the discharge and the external circuit, and the volume charge that comes from the charged plasma particles. Then the Gauss' law takes the form

$$\oint_{S_i} \varepsilon_0 \boldsymbol{E} \cdot \boldsymbol{ds} = Q_i = \oint_{S_i} \sigma_i ds + \int_{Vol_i} \rho_i dV,$$

where σ_i is the surface charge density at point i, ρ_i is the charge density in the same point, and Vol_i is the volume of the box. This is equivalent to

$$\varepsilon E_{z\,i,1/2} = \frac{1}{2}\rho_i \, Vol_i + \sigma_i \tag{3.10}$$

By use of finite differences, $E_{z\,i,1/2}$ can be expressed as $(\Phi_0 - V_{i,1})/\Delta z$, where Φ_0 is the cathode potential. Rearranging (3.10) for σ_i and summation over all boxes i, yields an expression of the total surface charge density on the cathode (σ_T) as a function of the cathode potential (Φ_0), the potential values at the first grid point in the discharge, for all the boxes, i.e., radial positions ($V_{i,1}$), and the corresponding volume charge densities in these boxes [144].

Furthermore, (3.9) can be discretized with backward finite differences

$$A\left(\sigma_T^t - \sigma_T^{t-1}\right) = \left[I_{ext}\left(t\right) + I_{dish}\right]\Delta t \tag{3.11}$$

Then according to Kirchhoff's voltage loop law, the cathode potential, $\Phi_0 = V_{\text{ext}} - R_{\text{ext}} I_{\text{ext}}$. Expressing from there I_{ext} and introducing it to (3.11) produces

$$\sigma_T^t = \frac{1}{A}\left[(V_{ext} - \Phi_0)\frac{\Delta t}{R_{ext}} + Q_{dish}^t\right] + \sigma_T^{t-1} \tag{3.12}$$

Equation (3.12) can be combined with the equation for σ_{T} (obtained by rearranging (3.10); see above and [144]) in a single equation for Φ_0 as a function of the potentials, $V_{i,1}$ and charge densities, $\rho_{i,0}$ both taken in time t, and the total surface charge density at time $(t-1)$.

The problem here is that such an equation is at the same time a boundary condition for the Poisson's equation (3.7) (see above). This leads to the necessity that (3.7) must be solved iteratively until the boundary condition is fulfilled, which is extremely inefficient in computational sense. Alternatively, the potential at any grid point, $V_{i,j}$, can be expressed as a superposition of two other potentials

$$V_{i,j} = V_{i,j}^{\text{P}} + \Phi_0 V_{i,j}^{\text{L}}. \tag{3.13}$$

The potential, $V_{i,j}^{\text{P}}$, is a result solely of the presence of charges inside the magnetron. Thus, it is a solution of (3.7) with boundary conditions $v_{i\,0}^{\text{P}} = V_{i,nz}^{\text{P}} = V_{nr,j}^{\text{P}} = 0$, where nr and nz represent the grid nodes located at the walls of the magnetron. The dimensionless potential, $V_{i,j}^{\text{L}}$, accounts for the influence of the cathode potential and is a solution of the Laplace equation $\Delta V_{i,j}^{\text{L}} = 0$ with boundary conditions $V_{i\leq nr_1,0}^{L} = 1$ and $V^{\text{L}} = 0$ at the walls. Replacing $V_{i,j}$ with (3.13) finally yields an expression for Φ_0 as a function of the potentials and charge densities in the plasma, in front of the cathode, at time t, the external (applied) potential, and the total surface charge density at time $(t-1)$.

$$\Phi_0 = \frac{-a_2 \sum_{i=0}^{nr_1-1} V_{i,1}^{\text{P}} - a_3 V_{nr_1,1}^{\text{P}} - a_4 \sum_{i=0}^{nr_1-1} \rho_{i,0} - a_5 \rho_{nr_1,0} + \frac{Q_{\text{disch}}^t}{A} + a_6 V_{\text{ext}} + \sigma_{\text{T}}^{t-1}}{a_1}, \tag{3.14}$$

where $a_1 - a_6$ are coefficients, dependent on geometrical factors and on $V_{i,j}^{\text{L}}$ [144].

In this way, Φ_0 at time t can be calculated only from known quantities at the same time. Then the overall procedure for simultaneous advance of the circuit and the discharge in time is as follows. In the beginning of the simulation, the Laplace equation is solved to determine $V_{i,j}^{\text{L}}$. Next, the coefficients a_1 through a_6 are calculated. These two steps are performed only once. Then at each time step, (3.7) is solved with zero boundary conditions to obtain $V_{i,j}^{\text{P}}$. With $V_{i,j}^{\text{L}}$ and $V_{i,j}^{\text{P}}$ known, (3.14) is solved for Φ_0. Afterward, (3.13) is used to produce the discrete potential distribution in the discharge $V_{i,j}$. Finally,

(3.12) is solved to get σ_{T}^{t}, which is going to be used in (3.14) during the next time step.

Finally, once the potential, $V_{i,j}$, is known, the electric field $\boldsymbol{E}$ is calculated from

$$\boldsymbol{E} = -\nabla V.$$

Force Interpolation and Smoothing

With $\boldsymbol{E}_{i,j}$ calculated above, the force $\boldsymbol{F}_{i,j}$ needs to be interpolated to the particle locations. This operation is known as *force interpolation* and is inversely identical to the charge assignment (see the section above). What is important is that the same shape factor must be used in both charge assignment and force interpolation. Not doing so usually results in a nonphysical self-force, i.e., a particle experiences a "force" caused by the particle itself [148, 153]. Using the same shape factor secures the total momentum conservation of the simulated system.

The procedure of weighting (charge assignment and force interpolation) introduces naturally fluctuations of the grid quantities. The amplitude and the density of the fluctuations are reversely proportional to the number of SPs per grid cell. In magnetrons, the charge distribution is very inhomogeneous (see Sect. 3.5.4 below). This results in a situation where in some grid cells the number of SPs is very small, which can cause strong fluctuations. These fluctuations can evolve in instabilities that can terminate the simulation or bring it to a nonphysical solution. To prevent that from happening, *digital filtering* or *smoothing* is needed. The smoothing can be described as the substitution of the grid quantities at every grid node with some-averaged (smoothed) values received by averaging the grid quantities at the adjacent grid nodes. Different methods exist for that. In the current simulation, after the charge assignment is finished the charge density is smoothed before being used for calculation of the potential.

There are many digital filters that in principle can be used [156, 157]. However, the filter must be isotropic to represent correctly the physical reality. Additionally, it must be computationally efficient because the filtering is performed at each time step. The filter, adopted in our work, uses the unfiltered values of the closest neighboring grid points (9-point filtering) [153]. It can be represented by the following transformation

$$\rho_{i,j}^{\mathrm{filtered}} \leftarrow \frac{4\rho_{i,j}^{\mathrm{raw}} + 2\left(\rho_{i-1,j}^{\mathrm{raw}} + \rho_{i+1,j}^{\mathrm{raw}} + \rho_{i,j-1}^{\mathrm{raw}} + \rho_{i,j+1}^{\mathrm{raw}}\right) + \rho_{i-1,j-1}^{\mathrm{raw}} + \rho_{i-1,j+1}^{\mathrm{raw}} + \rho_{i+1,j+1}^{\mathrm{raw}} + \rho_{i+1,j-1}^{\mathrm{raw}}}{16}$$

Stability and Accuracy of the PIC Model

The PIC model is a discrete approximation of a continuous physical picture. As such, it always introduces a numerical noise. The magnitude of this noise reaches zero only when the number of SPs per grid cell approaches the number

of real particles in the same grid cell. Therefore, all kinds of particle simulations are by definition noisy in contrast to fluid models. The noise, however, should be kept under a certain maximum level to have meaningful results. More importantly, the error introduced by the noise must not be allowed to grow with the simulation. Several factors directly influence the noise. These include the time step, the number of SPs per grid cell, the shape factor, and the grid size. The specific mechanism through which this influence is manifested depends on the type of the numerical integrator of the equation of motion. In our model, the leapfrog integrator is implemented. A quantitative analysis for the error introduced by this method is given in [144]. It is found that the standard leapfrog algorithm has a quadratic error term for $\omega_0 \Delta t \ll 1$, where ω_0 is the characteristic frequency in the simulated system. In DC magnetrons, the two highest frequencies are the electron plasma frequency

$$\omega_{\mathrm{pe}} = \sqrt{n_{\mathrm{e}} q_{\mathrm{e}}^2 / \varepsilon_0 m_{\mathrm{e}}}$$

and the electron gyro frequency, ω_{ce}, given by $\omega_c \equiv |q|B/m$.

Hence, $\omega_0 = \max\{\omega_{\mathrm{pe}}, \omega_{\mathrm{ce}}\}$.

It should be emphasized that the error is cumulative with the number of time steps. This means that the longer the simulation is run, the bigger the overall error is. Consequently, the following paradox exists. Setting the tolerable error too small limits the number of time steps. Allowing a large number of time steps increases the error as the cube of the time step [153]. In the literature, a common compromise has been set

$$\omega_0 \Delta t \approx 0.2 \tag{3.15}$$

In magnetrons, the standard leapfrog algorithm is expanded to deal with the magnetic field and the rotation caused by that field. Thus, it is important to keep the calculated rotational angle reasonably close to the real one. An analysis of this problem can be found in [148]. It shows that for magnetic field strengths of interest the condition (3.15) secures that the rotation term of the equation of motion (see section "Integration of the Equation of Motion") is calculated with an error not exceeding that of the general leapfrog algorithm. The exact condition is

$$\omega_0 \Delta t < 0.35. \tag{3.16}$$

Generally, in two and three dimensions, the discussion for the stability and accuracy is much more complex. However, when one of the dimensions is dominant and the stability is achieved for it, it can be accepted that the whole simulation is stable. Typically, the dominant dimension is in the direction of the strongest gradient of the electric field. For our magnetron simulations, it is the z-direction. In line with that, the *Courant criterion* [158] is

$$v_k \Delta t_k / \Delta z \leq 1, \tag{3.17}$$

where v_k is the characteristic velocity of the kth type of SPs and Δt_k is its time step. The meaning is that, if (3.17) is violated, too many SPs are jumping

over field variations, which leads to numerical heating. Thus for a given Δt, defined by (3.16), the formula (3.17) sets a bottom limit for the grid size, Δz. At the same time, the grid must be fine enough to resolve the sheath. This leads to the upper limit for Δz

$$\Delta z \leq \lambda_{\mathrm{D}}, \tag{3.18}$$

where λ_{D} is the Debye length.

Relations (3.15), (3.17) and (3.18) define the stability and accuracy domain in terms of time step and grid size for the standard PIC simulation. Adding to that the MCC method (see below) will bring some additional conditions. More details about that are given at the end of Sect. 3.5.2. Modifications of the stability criteria with respect to speeding up the procedure are presented in Sect. 3.5.3.

3.5.2 Monte Carlo Collision Method

The PIC method has been originally designed to model collisionless plasmas. In magnetrons, as in other types of glow discharges, collisions sustain the discharge. Therefore, a numerical model must be able to incorporate them. This can be achieved by coupling the PIC model with a Monte Carlo collision (MCC) model. This means that at a certain moment of the time step the SPs should be checked for collisions. The coupling is not just a numerical trick made to account somehow for the collisions. It has sound physical grounds, which follow from the Boltzmann equation [144].

The collision probability for all individual SPs needs to be calculated during every time step. Let us consider here the electrons as example of the SPs. It can be proven [159] that the probability, P_i, for the ith electron to collide binary with any of the particles of type g (gas atom, for example) during time Δt agrees with the probability received from the elementary free-path theory [160]. That is

$$P_i = \nu \Delta t,$$

where ν is the collision rate given by $\nu = n_{\mathrm{g}} \bar{g} \sigma_{\mathrm{T}}$ with n_{g} being the target density, $\bar{g}$ the average relative speed between the ith electron and the target particles, and σ_{T} is the total cross section. In case of big disparity between the speed of the colliding particle, v_i, and the mean speed of the target particles, a common approximation is $\bar{g} \approx v_i$.

The cross section and therefore the collision rate are generally energy dependent. Since the velocities of the particles change with time, the collision rate is also time dependent. The probability, Q, that an electron, starting at time $t = 0$, does not collide in the interval $(0, t + \Delta t)$ is

$$Q(t + \Delta t) = Q(t)[1 - \nu(t \Delta t)],$$

where the term in the square brackets is the probability for no collision in the interval $(t, t + \Delta t)$. When $\Delta t \to 0$, this equation becomes

$$\frac{\mathrm{d}Q}{\mathrm{d}t} = -\nu(t)Q(t)$$

with a solution

$$Q(t) = \exp\left[-\int_0^t \nu(t)\mathrm{d}t\right]. \tag{3.19}$$

Consequently, the probability that a collision takes place within a time $t = t_c$, is given by:

$$\mathrm{Prob}\{t_c\} = 1 - Q(t_c).$$

This probability is calculated by generating a uniformly distributed random number (U) in the interval [0,1] [161]

$$1 - Q(t_c) = U. \tag{3.20}$$

Hence, once U is generated, the time t_c, which defines when a collision takes place, can be calculated from (3.19) and (3.20). This constitutes the general Monte Carlo procedure for determining whether a collision takes place. However, it is impractical, unless the collision rate is constant.

Instead, the *null-collision method*, first introduced by Scullerud [162], can be used. Its main feature is the introduction of a constant maximum collision frequency, $\nu_{\max}$, that is always higher than $\nu(t)$ for any t. Hence, when (3.19) and (3.20) are solved with $\nu_{\max}$ instead of ν, the solution is

$$t_c' = -\nu_{\max}^{-1} \ln U. \tag{3.21}$$

To find a relation between t_c and t_c', the same U should be used. Then according to (3.20), $t_c' < t_c$. The collision probabilities for ν and $\nu_{\max}$, respectively, at time, $t = t_c'$, are

$$P_c = 1 - \exp\left[-\int_0^{t_c'} \nu(t)\mathrm{d}t\right],$$

$$(P_c)_{\max} = 1 - \exp(-\nu_{\max} t_c'). \tag{3.22}$$

Consequently, the probability that a collision is regarded real, i.e., it really happens in the model, is equal to $P_c/(P_c)_{\max}$. Note that the condition, $P_c < (P_c)_{\max}$, is always fulfilled.

The efficiency of the method arises from the fact that there is no need to calculate the actual collision time t_c in (3.20). If t_c' is small enough, which is always true if the time step of PIC is used, the collision rate can be

approximated with a quadratic polynomial. Then the integral in the first of (3.22) becomes [139]

$$\int_0^{t_c'} v(t)\mathrm{d}t = \frac{t_c'}{6}\left[v(0) + 4v(t_c'/2) + v(t_c')\right]. \tag{3.23}$$

Equation (3.23) can be used to determine the probability for collision from (3.22).

So far, the total probability of collision, P_T has been discussed. When there are m types of collision, all possible in the time interval of interest, the probability for the kth type of collision ($0 < k \leq m$), characterized by a collision rate v_k is given by

$$P_k = 1 - \exp\left[-\int_0^{t_c'} v_k(t)\mathrm{d}t\right]$$

and

$$P_T = \sum_{k=1}^{m} P_k. \tag{3.24}$$

Then the sampling of the kth collisional event is made with a probability of P_k/P_T.

The drawbacks of the null-collision method are connected to the implicit condition that the particles in the ensemble have the same collision rates. Or, what is equivalent, that their mean collision path is the same. Such situation is easily realized in a uniform electric field, for instance. That is why the method is especially efficient in swarm calculations. Its application to PIC simulations has been introduced by Vahedi and Surendra [163]. However, no theoretical analysis has been carried out to determine what strengths of the electric field gradients are allowed for the stability domain of the null-collision method. In magnetrons, strong gradients in both electric and magnetic fields exist, and as it has already been pointed out, the whole magnetron plasma is very inhomogeneous. The amplitude of the electric field gradients is proportional to the strength and geometry of the magnetic field. All this makes the use of the null-collision method in magnetron modeling highly questionable, especially at strong magnetic fields. An additional problem may appear from the selection of the particles (especially the electrons) which are considered for collision in each time step. The procedure of Vahedi and Surendra [163] requires the determination of some maximum number of particles eligible for collision. It is intuitively clear that when the particles are with small dispersion in their velocity distribution they can be selected randomly. Unfortunately, the latter is not the case in magnetrons, where a relatively small number of electrons are responsible for the main processes that sustain the discharge. Consequently, if the colliding electrons are selected purely on random basis it can lead to underestimation of the collisions of the "important" group of electrons.

The above discussion motivates the introduction of a collision sampling procedure, both capable of dealing with strongly inhomogeneous velocity and spatial distributions and which is computationally effective. Such a procedure has been developed by Nanbu [164]. It makes it possible by use of a single random number to determine not only whether a collision occurs, but also what type of collision takes place. In this way, the computational efficiency is significantly improved. The checking is done on per particle basis, which ensures the equal treatment of all particles. For the case of electron-neutral collisions, where the speed of the neutrals is neglected and they are considered homogeneously distributed in space with a density, n_g, the procedure is as follows.

The total probability for collision is given by (3.24), where

$$P_k = n_g v \sigma_k \Delta t. \tag{3.25}$$

Here, v is the electron speed. Equation (3.24) can be rewritten as

$$1 = P_T + (1 - P_T) = \sum_{k=1}^{m} \left[P_k + \left(\frac{1}{m} - P_k \right) \right],$$

which is visualized in Fig. 3.10.

The unit length is divided into m equal intervals, where m stands for the number of different collision types. Each interval has two parts. In the kth interval, e.g., the left part has a length equal to $1/m - P_k$ and the right side is P_k. The sum of the right parts of all m intervals equals the total collision probability, P_T and the sum of the left parts gives the probability of no collision, $1 - P_T$. The procedure is to generate a uniformly distributed random number $U \in [0, 1]$. The integral part of $mU+1$ specifies the kth interval corresponding to the kth collisional event, i.e., $k = \text{int}[mU + 1]$. Then only P_k needs to be calculated, which is a significant speed-up in case of big m. Finally, the same U is checked to see in which part of the kth interval it falls. If

$$U > \frac{k}{m} - P_k$$

holds, the kth collisional event occurs. If not, no collision takes place.

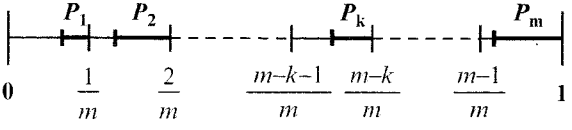

Fig. 3.10. Visualization of the Nanbu's method [162] for sampling a collisional event. The right-hand side of the kth interval (drawn with *thicker lines*) represents the probability of the kth type of collision. The sum of the left-hand sides of all intervals (represented by *thinner lines*) is equal to the probability of no collision. The sum of the right-hand sides equals the total collision probability, P_T

In all MCC algorithms, the collisional time step, Δt_c, must be small enough in order not to miss a real collision. This condition stems from the fact that for one time step, the colliding particle is allowed to undergo at maximum one collision. For the Nanbu's method, this condition is $P_k < 1/m$ for all m, for all electron energies. The electron energies in DC magnetrons are restricted approximately to the energy equivalent of the applied voltage. Then some $P_{\max}$ can be estimated, that corresponds to the biggest cross section, $\sigma_{\max}$, of all the included processes for all the possible energies. Then the maximum allowed Δt_c can be obtained from (3.25) with σ_k replaced by $\sigma_{\max}$ and $P_k = 1/m$. This is practically not a limitation at all, when the method is used in PIC simulations, because the general time step limitation of PIC is more restrictive (see above (3.16)).

The coupling of the collision check with the PIC cycle can be done in different moments inside the time step. Our choice is to check for a collision in the middle of the time step. This choice has been dictated by the time centering of the leapfrog integrator (see section "Integration of the Equation of Motion", and especially Fig. 3.5). At this moment, the positions of the particles are exactly known. At the same time, only half of the acceleration is applied. The rotation may or may not be calculated. It does not matter, because the rotation does not change the speed and hence the energy of the colliding particle. Therefore, the energy is also known at the middle of the time step, though the velocity is unknown.

The inclusion of the MCC module to the PIC method is shown schematically in Fig. 3.11. In case of collisions, the precollision velocity of the colliding particle is replaced by its postcollision velocity, which is determined based on the fundamental laws of conservation of energy and momentum during collision, plus geometrical considerations related to the particle's orientation before the collision, as is explained in detail in [144], for the different types of collisions (electron-neutral, ion-neutral, neutral-neutral, and Coulomb collisions).

3.5.3 Methods for Speeding Up the Calculations

As already mentioned before, PIC-MCC simulations of DC magnetrons are very time-consuming. This is caused by two main factors. The first one is the relatively high plasma density leading to a large number of SPs that need to be simulated. The second one is the time needed for convergence to be achieved. The simulation should be run for at least 10^{-5} s, which is the relaxation time in a DC glow discharge [165]. The high plasma density limits the allowed time step, which results in a large number of time steps (computational cycles) that should be performed to reach the 10^{-5} s limit. All this motivates the incorporation of computational techniques and physical approximations that can alleviate the computational load. Here, an overview of the methods, used to achieve this goal, is given.

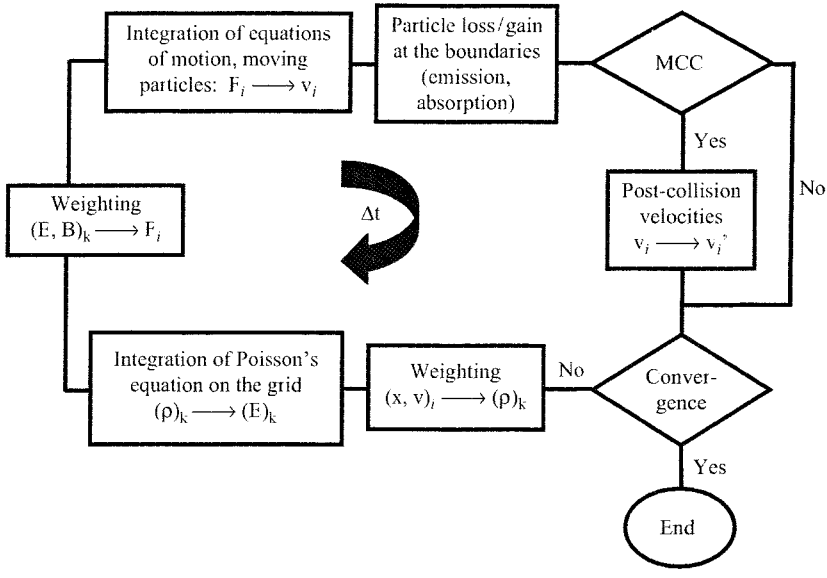

Fig. 3.11. Scheme of a PIC-MCC cycle. The collision check is performed at time $t + (1/2)\Delta t$. The notation v_i' refers to the postcollision velocity of the ith particle. All other symbols are as in Fig. 3.4

Subcycling

Subcycling [158] is the partial advance of the simulated system. This means that different parts of the system are advanced with different time steps. The fast evolving components are normally advanced a fixed number of times per one evolution of the slow components. If the system time step, and therefore the main cycle, is those of the slower components, then the fast ones are moved several times within the main cycle. Or in other words, they are subcycled. The fast particles that require the smallest time step (see section "Stability and Accuracy of the PIC Model") are the electrons. Ions are roughly 2,000 times heavier than electrons and hardly move during an electron time step. This allows, according to the stability and accuracy criteria of the PIC method, that they can be advanced safely once per 20–50 electron time steps. The electric field, however, is recalculated after each electron time step. In this sense, the term subcycling is to some extent a misnomer in the present study.

Variable Time Step

The initial density, loaded in the beginning of the simulation, is much lower than the density in a steady state. The time step restriction [(3.16)] must be obeyed at any time. Since the plasma density changes, so can the time step.

The classical approach is to fix the time step to obey (3.16) for the maximum expected density. This is a simple and safe decision from a programmer's

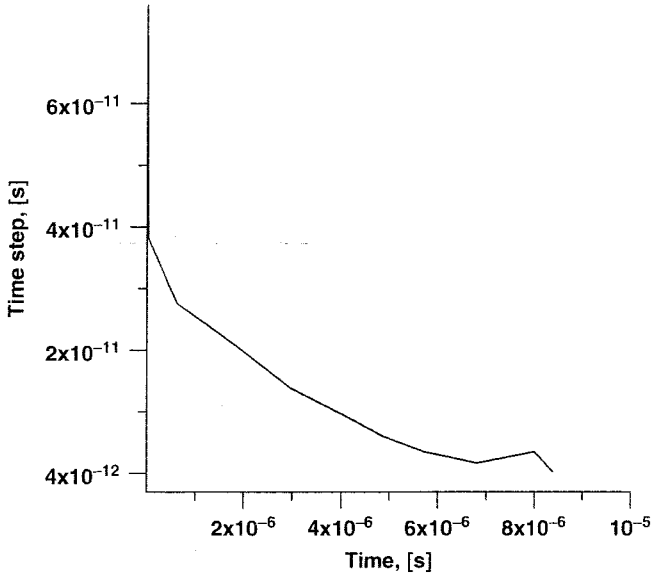

Fig. 3.12. Adapting of the time step throughout a typical simulation

point of view, but is computationally ineffective, because unnecessary small time steps are used in the initial stage of the simulation when the discharge is being built up and the plasma density is low. Alternatively, we choose to use a variable time step. This is done in the following way. At the beginning, the time step is set to satisfy (3.16) for the initial electron density. Afterward, at every 5,000 time steps the maximum electron density in the discharge is found and if (3.16) does not hold anymore, the time step is increased by 25%. This is illustrated in Fig. 3.12, where the time evolution of the time step in a typical simulation is shown. As it is seen, during a significant part of the simulation, the time step is larger than the steady state time step. This allows decreasing the necessary number of computational cycles, and hence the overall computation time, by 30–40%.

Optimization of the Weighting

The weighting has been discussed in previous sections "Charge Assignment" and "Force Interpolation and Smoothing". Each particle should be assigned to the four NGPs at every time step. If the coordinates of the particles are stored in physical units for distance, a floating-point division should be performed to determine to which cell the particle belongs. This is computationally very costly. Instead, the coordinates of the particles are stored in terms of grid cells. For example, if the ith particle has a coordinate, $r = 3.356$ expressed in cell units, rather than in meters, the determination of the cell in which the particle is located is done by simply taking the integer part of the coordinate.

The remaining part specifies the location of the particle inside the cell. When the real coordinate of the particle is needed, a multiplication is performed, which is computationally more effective than a division.

Sorting

In the classical form of the PIC method, the simulated particles of a given type are indistinguishable. Each particle is just an element of an array. The position of the particle in this array, i.e., its number, is arbitrary and does not provide any specific information for the particle. This means that there is no correlation between the position of the particle in the array, and the particle's location in the coordinate space. This organization is somehow natural to understand and straightforward to program. The addition of the MCC technique fits into this scheme if the collisions are only between the given type of particles and the background gas, which is homogeneously distributed in the velocity and coordinate space. Examples for such collisions are the electron-argon atom collisions. In any other type of collisions (e.g., Coulomb collisions), a collision partner must be found, based on its spatial location. One way to do that is to perform a search among all the particles and to find all collision candidates that are in the vicinity of the incident particle. The usual method here is to approximate this vicinity to the cell in which the incident particle is located. Such procedure is, however, computationally very inefficient.

Alternatively, if the array of the particles is not randomly formed, but ordered in such a way that the number in the array is in direct relation to the cell where the particle is located, finding a collision partner will be much faster. The ordering of the particles in such a way is called *sorting*. It not only facilitates the calculation of collisions, but also has a strong, positive side effect. It speeds up the entire PIC-MCC simulation. This acceleration is in relation with the architecture of the modern computers, as is explained in [144]. It has been reported [166] that for a 2d3v PIC simulation the calculation time decreases with 40–70% when sorting is implemented.

Algorithms for ordering of data can be found in text books of numerical methods [167,168]. However, common sorting techniques are very slow at sorting large arrays of particles, which is the case in a PIC-MCC simulation of a DC magnetron. For example, a *quicksort*, which is an "in place sort algorithm" [168], needs to pass through the particles approximately $\log_2 N$ times, where N is the number of particles. This leads to the impressive $8kN \log_2 N$ floating point memory loads and stores for the case of a 2d3v PIC-MCC simulation with k types of particles. This inefficiency is a result of the fact that most of the well-known sorting algorithms originate from the past, when the amount of memory has been the main restriction. Contemporary workstations offer sufficient amount of memory and thus there is no need for in place algorithms (algorithms that order an array without using auxiliary arrays). Therefore, we used the "out of place sorting algorithm" [166], as is explained in detail in [144].

Different Weights for Different Types of Particles

Depending on the aim of the particular magnetron simulation, different plasma species can be included that can have rather different number densities. For example, while the electrons and argon ions have always similar densities, the density of the sputtered atoms and fast argon atoms is typically one to three orders of magnitude higher. In this case, it is not feasible to use the same weight for the neutrals and for the charged particles. The condition that the minimum number of followed particles must be such that there are at least several SPs per Debye sphere, combined with the demand for maximal speed of the calculations, determines the weight of the SPs representing the real type of particles with the lowest density. The weight of the SPs representing the real particles with higher density is chosen also higher. How much higher is determined from the practical consideration that the number of SPs from each type must be similar. Using different weights allows obtaining the necessary statistical representation, without paying the price of following an unnecessary large number of SPs.

The implementation of different weights is trivial in a PIC code. When a MCC method is added, however, there are two cases. The first one is when plasma species collide with the uniformly distributed background gas, or when they collide with other plasma species with the same weight. In this case, the procedure is the same as when all SPs are equally weighted, because the weight is anyway included in the charge assignment and force interpolation. The second case includes collisions between SPs with different weight. This requires an additional treatment, as explained in detail in [144]. The guiding principle here is that the SPs represent real particles, and all physical relations between the physical particles must be correctly represented by the SPs.

3.5.4 Examples of Calculation Results

Operating Conditions and Simulation Data

In this section, the PIC-MCC model described in Sect. 3.5, will be applied to a laboratory magnetron, Von Ardenne PPS 50 (see below), operated in argon with a copper cathode, to illustrate the type of results calculated with this model. This includes, among others, the distribution of the electric field and potential, the densities of the plasma species and their energy distribution functions, and the erosion profile as a result of cathode sputtering. The calculation results will be quantitatively compared with existing experimental and numerical data.

The scheme of the planar magnetron used for the calculations is shown in Fig. 3.13. It is a Von Ardenne PPS 50 magnetron (commercially available), used with plasma shield (the sidewall on the scheme in Fig. 3.13). The axisymmetric magnetic field is created by two concentric magnets located under the powered electrode, i.e., the cathode. The magnetron is balanced, which means

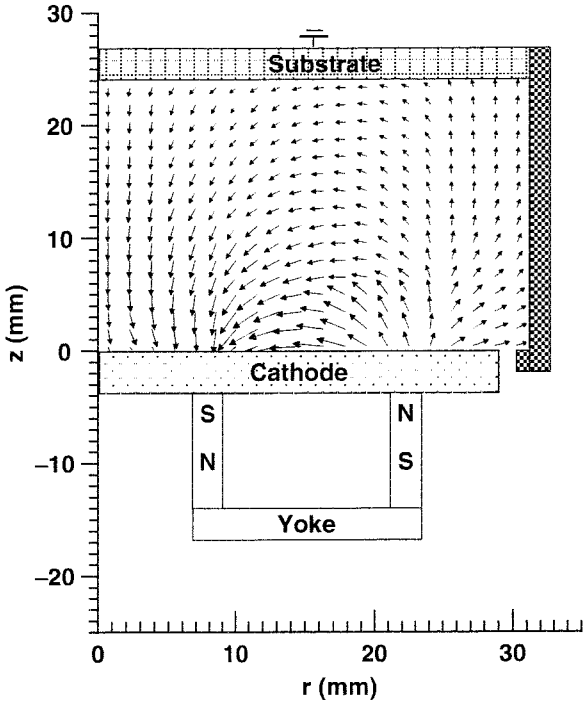

Fig. 3.13. Scheme of the magnetron Von Ardenne PPS 50 with the spatial distribution of the (measured) magnetic field. The scheme is axisymmetrical relative to the axis, $r = 0$

that the majority of the magnetic flux lines originates at and returns to the cathode surface without crossing the anode.

All walls, except the cathode, are grounded and act as an anode. The smallest separation between the electrodes is equal to 2 mm and the distance between the cathode and the opposite anode plate, where the substrate is mounted, is 24 mm. The cathode is a copper disk with a thickness of 3 mm and a diameter of 58 mm. The discharge is maintained by a DC power supply, which can be run in a constant current or in a constant voltage mode. The magnetic field used in the simulation has been experimentally measured when the discharge has been not operational. In the simulation, the external circuit shown in Fig. 3.8 above, is connected to the cathode.

In this numerical study, the magnetron plasma consists of argon atoms, singly charged argon ions and electrons only. All other plasma species are excluded from the analysis. In addition, the argon atoms are considered homogeneously distributed at room temperature (300 K). The choice of these plasma species is dictated from the fact that they are the dominant ingredients and play the main role for the formation and maintenance of the discharge.

The influence of the sputtered atoms and the presence of the nonequilibrium argon atoms will be discussed in Sect. 3.6 below.

The collisions that are taken into consideration are electron elastic scattering from the argon atoms, electron- and ion-induced excitation and single ionization of the argon atoms, and elastic scattering of argon ions from their parent atoms. The last process includes isotropic scattering and charge transfer. The excited argon atoms are not followed in this simulation. The process of their formation, however, is important for a correct representation of the energy balance. In the case of electrons, it also contributes to the conductivity of the discharge, since the electrons cross the magnetic field lines due to collisions. Because the main excitation levels of the argon atom are very closely located in terms of energy [169], all electron-impact excitation processes are grouped into a single collision with an energy loss for the electrons of 11.55 eV. This is done to limit the computational time. The cross sections of the above-mentioned collisions have been adopted from the literature [169–173], and can be found back, plotted as a function of energy, in [144]. At the walls, besides sputtering and secondary electron emission, also recapture of electrons at the cathode is included (see also the previous section).

The maximum number of the SPs in this simulation is two millions, i.e., one million electrons and one million argon ions. In the beginning of the simulation, they are loaded with uniform density in the coordinate space and with a Maxwellian distribution in the velocity space. The initial density equals $3 \times 10^{14}\,\mathrm{m}^{-3}$. The external circuit is set with a resistor of 1,200 kΩ and with a constant voltage source of −800 V. This corresponds to typical experimental values of this type of magnetron. The maximum magnetic field is 0.045 T. The computational grid has 241 nodes in z-direction and 129 nodes in r-direction. The initial time step is set to 3×10^{-10} s. The number of electron subcycles per ion cycle is 25. The simulation is run until convergence is obtained in terms of cathode potential and particles' densities. This is illustrated in Fig. 3.14, where the time evolution of the cathode potential, Φ_0, is shown. Note that, although the external applied voltage is equal to −800 V, the voltage drop across the magnetron discharge is only about −330 V. The gas pressure for this example of simulation results is kept fixed at 0.67 Pa.

Calculated Potential and Electric Field Distribution

The calculated potential distribution is shown in Fig. 3.15. It has a clearly expressed radial dependence, which follows the pattern of the magnetic field. The gradient in the potential is steepest near the cathode (i.e., in the sheath, see below), and at about $r = 18.2$ mm, where the radial component, B_r, of the magnetic field has a maximum. Above the center of the cathode, where the magnetic field lines are perpendicular to the cathode surface (see Fig. 3.13), the potential shape is identical to that of a nonmagnetized discharge. As a whole, the plasma potential is negative almost in the entire discharge, i.e., the discharge operates in a negative space charge mode. This

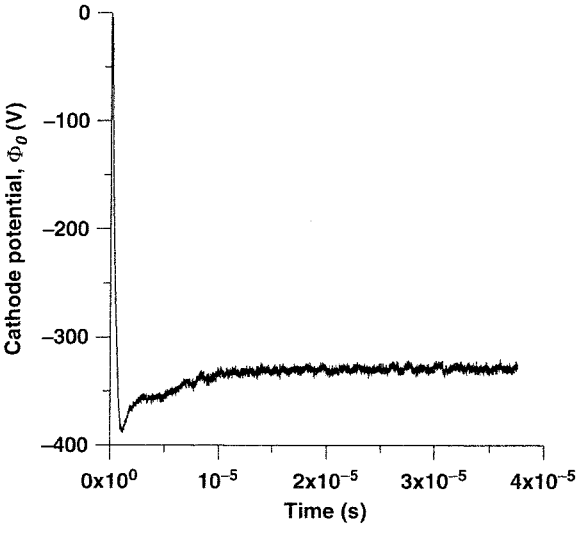

Fig. 3.14. Relaxation of the calculated cathode potential, Φ_0, with the physical time of the simulated system. The convergence occurs at time, $t \sim 12\,\mu s$

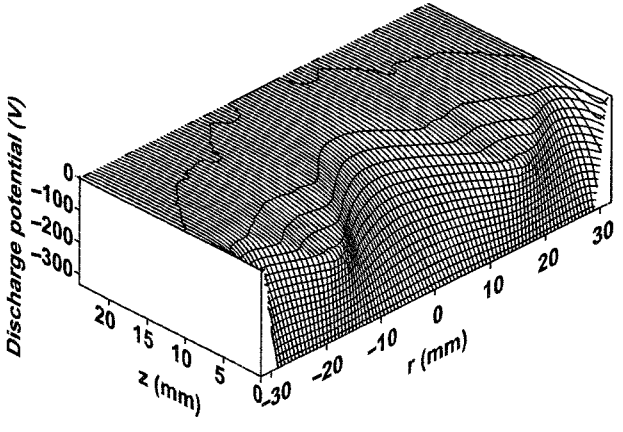

Fig. 3.15. Calculated potential distribution

is in accordance with analytical models [46, 62], a 1d PIC-MCC simulation of a cylindrical postmagnetron [36], and experimental measurements at similar operating conditions [174].

The sheath architecture can also be seen in Fig. 3.15. The sheath itself should be redefined in the case of magnetrons. In nonmagnetized glow discharges, the sheath boundary is frequently defined at the line, which separates the negative from the positive values of the potential. This definition works well in discharges operated in positive space charge mode. In mag-

netrons, however, the sheath border should be defined as a line where the potential has a well-pronounced inflexion. After the sheath, the next part of the potential can be defined as a presheath. This region is still characterized by a negative space charge and a relatively small electric field (in comparison to the sheath). This presheath is totally absent in discharges with positive space charge. The reason for appearance of the negative space charge and the presheath is in the restricted mobility of the electrons, due to the magnetic confinement. The potential distribution from Fig. 3.15 creates an electrical field, which axial and radial components are shown in Figs. 3.16 and 3.17, respectively.

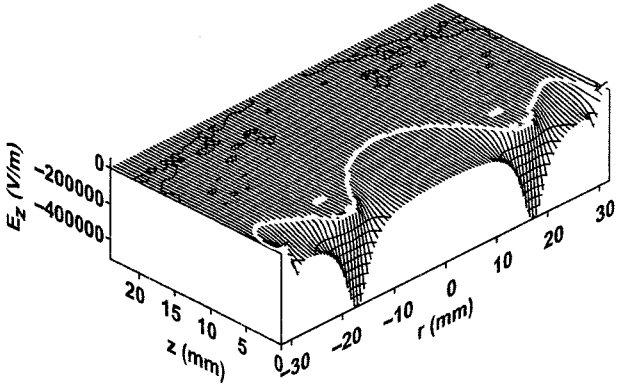

Fig. 3.16. Axial component, E_z, of the electric field. The white line corresponds to $E_z = 10\,\mathrm{kV\ m^{-1}}$ and may be considered as the end of the sheath

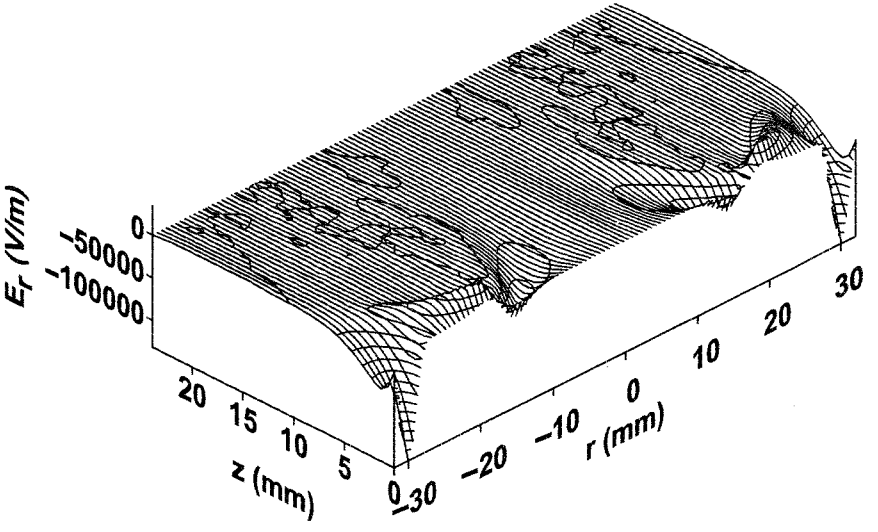

Fig. 3.17. Radial component, E_r, of the electric field

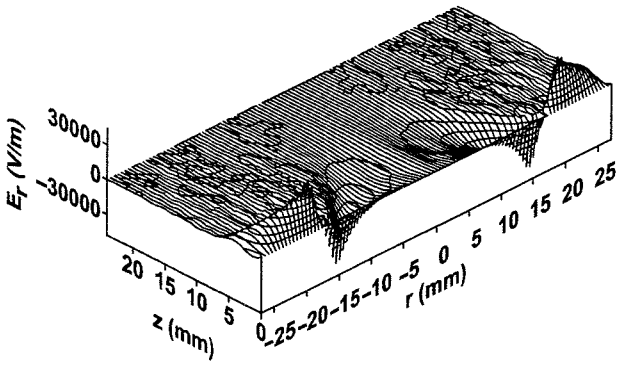

Fig. 3.18. Radial component of the electric field, E_r, in the region $r \leq 25\,\mathrm{mm}$

The magnitude of the axial field, E_z, is approximately ten times stronger than the magnitude of the radial field, except in the proximity of the gap between the cathode and the sidewall. In the sheath region above the racetrack, E_z approaches $500\,\mathrm{kV\ m^{-1}}$. The sheath border with its strong radial dependence is represented by the white line in Fig. 3.16. Along it, the magnitude of the field is approximately $10\,\mathrm{kV\ m^{-1}}$. The sheath thickness is only 1.6 mm above the racetrack, whereas at $r = 0$ it is about 13 mm. The sheath is thinnest and E_z strongest exactly in the middle between the magnetic poles ($r = 18.2\,\mathrm{mm}$).

The radial field, E_r, changes in the sheath. The field is strongest near $r = r_{\max}$, where the gap between the cathode and the grounded side wall is located. The structure of E_r is such that the region where $E_r > 0$ repels the electrons outward, whereas the region $E_r < 0$ accelerates the electrons outward. This has an effect of electrostatic trap, which enhances the magnetic confinement. The "valley-mountain" structure of E_r is more clearly seen in Fig. 3.18, where the region of the discharge away from the sidewall is shown.

Calculated Electron and Ar^+ Ion Densities

Figure 3.19 shows the calculated electron density profile. Most electrons are strongly confined between the magnetic poles. The calculated density profile reproduces satisfactorily the experimental data obtained by Langmuir probe measurements. For example, the calculated peak value at $p = 5\,\mathrm{mTorr}$ is $1.6 \times 10^{17}\,\mathrm{m^{-3}}$, whereas in [174] it is $9 \times 10^{16}\,\mathrm{m^{-3}}$ at $p = 2\,\mathrm{mTorr}$. The plasma decay with the distance from the cathode, as well as the radial variation of the electron density, agree very well with the data reported in [172] for $p = 5\,\mathrm{mTorr}$. The plasma distribution has a distinctive maximum at $z = 1.2\,\mathrm{mm}$.

Except in the sheath, the Ar^+ ion density profile is identical to the electron density profile. This is so, because although the ions are not magnetized, and therefore not magnetically trapped, they are electrostatically bound to the electrons. The Ar^+ ion density profile has a maximum at the same spot as

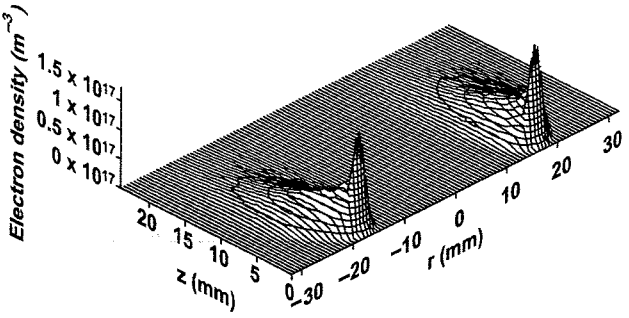

Fig. 3.19. Calculated electron density

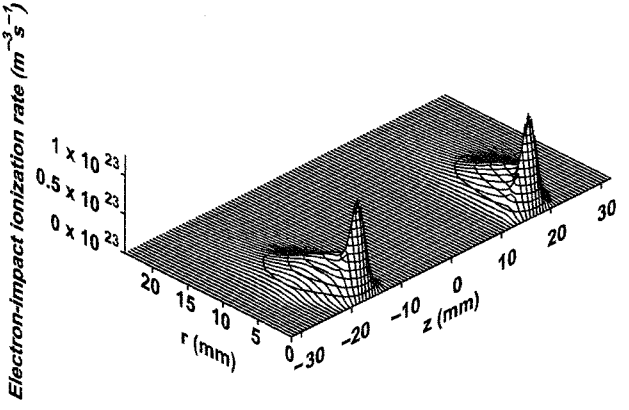

Fig. 3.20. Calculated profile of the electron-impact ionization rate

the maximum of the electron density. In the sheath, the Ar^+ ion density is nonzero, in contrast to the electron density. This gives rise to a positive space charge, and hence strong gradients in the potential distribution and axial electric field distribution.

Calculated Collision Rates

For the sustainment of the discharge, ionization of the argon atoms is crucial. In the present model, ionization is carried out by electrons and Ar^+ ions. The calculated electron-impact ionization rate is illustrated in Fig. 3.20. The Ar^+-impact ionization rate is not shown, because it is of minor importance at the operating conditions investigated. It is present only in the sheath where the ions can gain enough energy from the electric field to ionize the atoms [144]. Its peak ($5 \times 10^{21}\,\mathrm{m^{-3}\,s^{-1}}$) is about 1.5 order of magnitude lower than the peak of the electron-impact ionization ($1.2 \times 10^{23}\,\mathrm{m^{-3}\,s^{-1}}$). Integrated over the whole computational domain, electron-impact ionization is about 800 times more

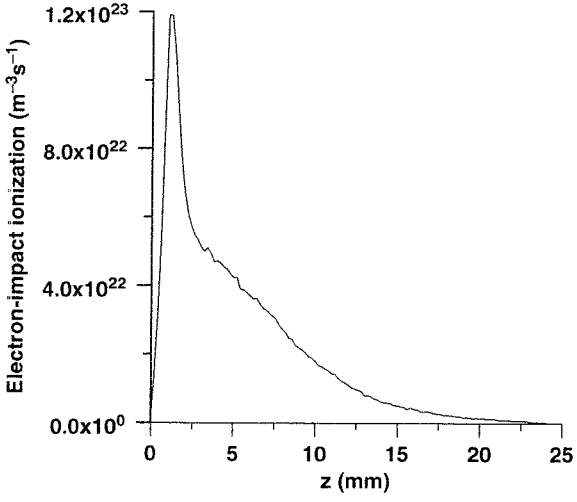

Fig. 3.21. Calculated electron-impact ionization rate, as a function of distance from the cathode, above the racetrack at $r = 18.2$ mm

important than Ar^+-impact ionization. Therefore, with reasonable accuracy, the Ar^+-impact ionization can be omitted in models and estimates for the current operating conditions. This is like expected, in view of the low voltage across the magnetron. In DC nonmagnetized glow discharges, where the applied voltage is in the order of 1 kV, this process cannot be neglected for an accurate description of the discharge behavior [175].

The axial profile of the electron-impact ionization rate above the racetrack at $r = 18.2$ mm is shown in Fig. 3.21. It has a maximum at $z = 1$ mm, i.e., inside the sheath. Its closeness to the cathode can be explained with the magnetic confinement. The Larmor radius for electrons with a speed of 10^7 m s^{-1} in a magnetic field of 450 G is 1.26 mm. This means that the electrons, ejected from the cathode, stay long enough in a hemisphere, which center is on the cathode and with a diameter equal to the Larmor radius. The electrons have an energy, which is optimal for ionization, before reaching the surface of the hemisphere. The shape of the ionization profile shows that most of the ionization is carried out by the primary electrons, originating at the cathode, rather than by secondary electrons, created in ionization collisions. There is nevertheless a significant amount of ionization taking place in the presheath and even in the bulk plasma. The borders of the two regions are reflected in the two inflexion points of the ionization profile at $z \approx 4$ mm and $z \approx 14$ mm.

The rates of electron elastic collisions and electron-impact excitation are characterized by a similar profile as the electron-impact ionization rate, but a second maximum is observed at about $z = 2$–3 mm. This can be explained, because the mean electron energy in this region is around 10 eV, which gives

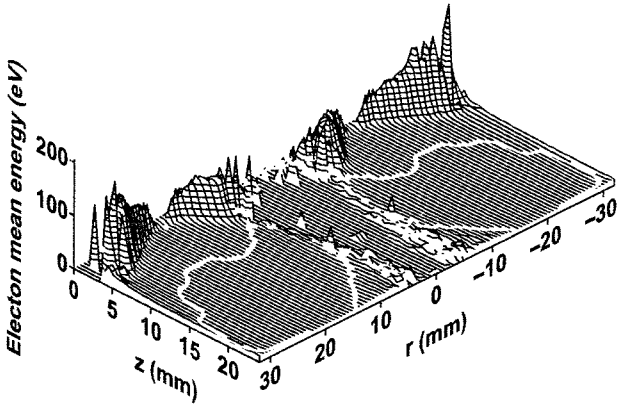

Fig. 3.22. Calculated mean energy of the electrons. Note that the z-axis is now reversed with respect to the previous figures, for the sake of clarity of the presented results. The cathode is still located at $z = 0$. The *white line* in the bulk corresponds to an energy of 10 eV

rise to a lot of elastic collisions and excitation, but which is a bit too low for efficient ionization.

Calculated Mean Energy and Energy Probability Function

The collision rates, together with the distribution of the electric and magnetic field determine the spatial distribution of the mean electron and ion energy and the corresponding energy probability functions. The calculated mean energy of the electrons is presented in Fig. 3.22. Note that the z-axis is reversed now, so that the energy spatial distribution is more clearly visible. Above the racetrack, where the electrons are strongly magnetized, their mean energy is about 40 eV. With radial displacement from the racetrack, the mean energy increases to 180 eV above the edges of the cathode. This increase is proportional to the weakening of the radial component of the magnetic field away from the centers of the magnets. Those electrons that enter the bulk are mostly with low energies, i.e., below the inelastic threshold. This fact, as well as the sharp transition of the mean energy profile to a plateau, immediately after the sheath, illustrates the effectiveness of the magnetron: the primary electrons are almost entirely utilized in ionization and excitation events before being lost. The region along the symmetry axis is strongly depleted from electrons, which is reflected by the "valley" in the mean electron energy profile.

The distribution of the Ar^+ ion mean energy (Fig. 3.23) follows the potential distribution. As it can be expected, the mean energy is high only in the sheath, with a maximum on the cathode surface. In the bulk, it is low, i.e., between 0.2 and 0.6 eV. The mean ion energy in the region between the

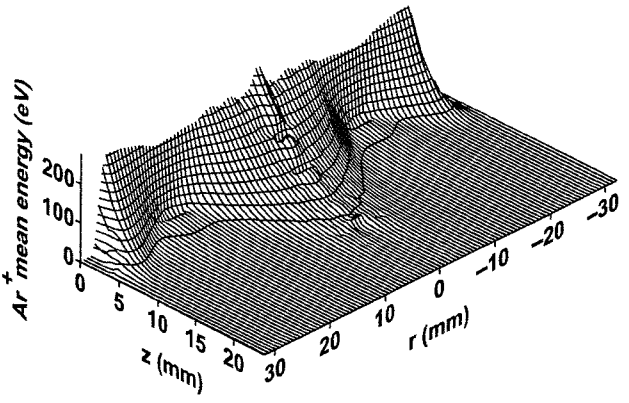

Fig. 3.23. Calculated mean Ar^+ ion energy. The cathode is located at $z = 0$

poles of the magnet is about 225 eV, which is approximately 70% of the cathode voltage. This ratio is slightly higher than the ratio of 60%, calculated in [116]. The difference can be explained from the broader sheath in [116], which allows the ions to spend more time in the sheath and consequently increases the probability for symmetric charge transfer collisions. These collisions are one of the two factors preventing the ions from obtaining energy values equal to the full cathode potential. The second factor is related to the location of the maximum of the ionization (see Fig. 3.20 above); it is between the sheath and the presheath. Thus, most of the produced ions accelerate in a potential difference that is less than the full interelectrode potential. All this shows that the common assumption of "freely falling ions" is not very accurate. Finally, in contrast to the electron mean energy, the ion mean energy does not have a radial minimum above the racetrack. This is a direct result from the fact that the ions are not magnetized.

The mean energy does not provide information about the population in the energy spectrum. Such information is given by the energy probability function (EPF), $f(\varepsilon)(= F(\varepsilon)\varepsilon^{-1/2})$, where $F(\varepsilon)$ is the energy distribution function and ε is the energy. The normalization of the EPF is: $\int f(\varepsilon)\varepsilon^{1/2}\mathrm{d}\varepsilon = 1$. The knowledge of the EPF also allows us to determine what the distribution of the velocities is and therefore to define a temperature, which allows simulated data to be compared with data received from probe measurements. As it has been already discussed, probe measurements are normally devoted to study the bulk plasma, because the sheath region compromises the accuracy of the probe readings [176]. For this reason, to compare our calculation results with experimental data, the quasilocal EPF has been sampled in the bulk in the present example. The sampling spot is a volume given by 14 mm $< z <$ 16 mm and 16 mm $< r <$ 20 mm. The calculated electron energy probability function (EEPF) is shown in Fig. 3.24. It represents practically a Maxwellian distribution with a temperature of 6.7 eV. Such a value is in good agreement with the spatial survey of magnetron plasma by means of a Langmuir probe [177]. In

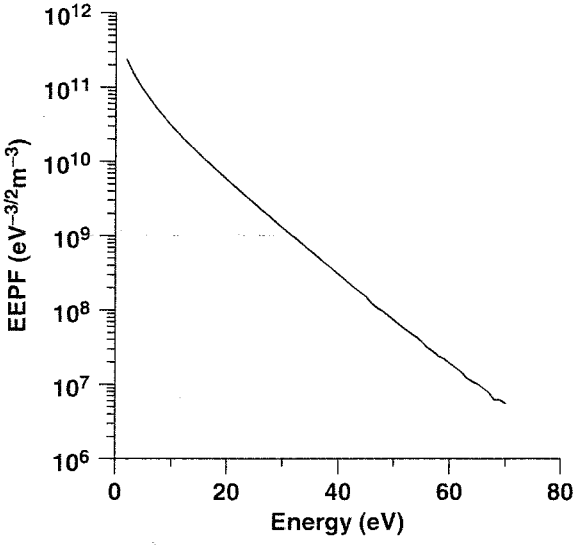

Fig. 3.24. Calculated electron energy probability function (EEPF) in the bulk (14 mm $< z <$ 16 mm, 16 mm $< r <$ 20 mm)

the latter experiments, for $p = 5$ mTorr, the electron temperature at $z = 3$ cm is found to be 5 eV and decreases with increase of z($T_e = 2.5$ eV at $z = 5$ cm). Therefore, our calculated T_e of 6.7 eV at $z = 1.5$ cm appears to be consistent with the experiment.

The Maxwellian distribution at such low pressure is a result of the magnetic confinement of the electrons, which secures enough collisions with the argon atoms before the electrons diffuse into the bulk.

There are reports in the literature for existence of two electron populations with different temperatures, which produces a Bi-Maxwellian distribution [178, 179]. More recent work [177], however, fails to confirm such phenomenon. The calculated results in the present example also do not indicate the existence of two electron populations with different temperatures.

The Ar^+ ions behave in a very different way than the electrons. Being practically not magnetized, the ions cannot stay for a long enough time in the discharge. This means they cannot suffer enough collisions for bringing them in equilibrium with the background gas. This is reflected in their EPF, shown in Fig. 3.25. As it is clear from this figure, the energy distribution is far from Maxwellian or other equilibrium distributions. In this case, the use of the temperature as a characteristic of the velocity distribution makes no sense. This result indicates that the use of fluid description for the plasma in DC magnetron discharges operated at standard conditions will not be correct. The same refers to hybrid models [110], where a Maxwellian distribution for the ions is normally assumed and they are treated as a continuum. The IEPF in Fig. 3.25 also questions the idea of measuring the ion temperature

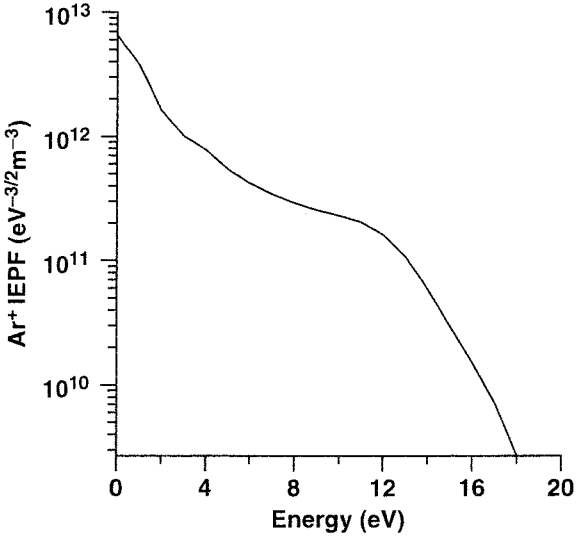

Fig. 3.25. Calculated Ar^+ ion energy probability function (IEPF) in the bulk (14 mm $< z <$ 16 mm, 16 mm $< r <$ 20 mm)

in DC magnetrons by probe experiments. In a more global aspect, the ion temperature does not bring any valuable information for the state of the plasma in DC magnetrons. It can only be used as mean ion energy, without providing any further insight for the velocity distribution.

Calculated Ion Flux Bombarding the Cathode

The Ar^+ ions that reach the sheath region or are created inside the sheath, accelerate toward the cathode, which they can bombard. This bombarding flux is responsible for the generation of primary electrons that sustain the discharge and for the sputtering. The rate of sputtering is proportional to the energy density of the bombarding flux. The spatial distribution of this flux at the cathode surface determines the sputtering region, i.e., the racetrack. Therefore, the knowledge of the flux is important, to predict the utilization of the target at given operating conditions. The calculated Ar^+ ion flux at the cathode is therefore presented in Fig. 3.26.

The flux is more or less limited to the region between the magnetic poles. This is in accordance with all experimental data, for instance for the erosion rate due to sputtering (see also Sect. 3.6). Its amplitude is proportional to the Ar^+ ion density. The localization of the flux, which follows the localization of the ion density in the radial direction, is a confirmation of the fact that the ions are practically not magnetized. Therefore, their movement in the sheath can be approximated as being directed toward the target, only disturbed by the collisions in the sheath.

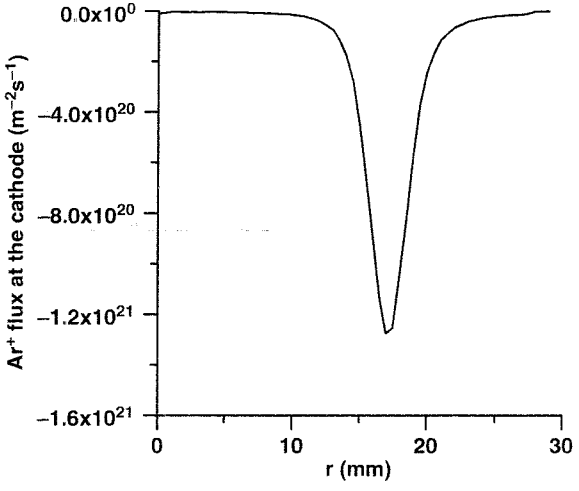

Fig. 3.26. Calculated Ar^+ ion flux at the cathode

As mentioned before, this Ar^+ ion flux gives rise to sputtering at the cathode (target). The behavior of sputtered atoms and corresponding ions, as well as of the Ar metastable atoms (which are important for the ionization of the sputtered atoms), will be described in Sect. 3.6.

3.6 Extension of the PIC-MCC Model: To Include Sputtering and Gas Heating

In Sect. 3.5, a detailed description has been given about the PIC-MCC model for an argon DC magnetron with copper cathode. The behavior of the sputtered copper atoms and corresponding ions was, however, not yet taken into account, because the Ar^+ ions and electrons are the dominant plasma species, determining the magnetron discharge behavior. However, to improve the application of sputter deposition, it is of course important to have a better insight in the behavior of the sputtered atoms. Therefore, the present section deals with an extension of the previously described PIC-MCC model to include the sputtered atoms and ions.

Moreover, it should be realized that the region in front of the cathode in a sputter magnetron is a highly dynamic region. Except the charged particles and equilibrium gas atoms, there exist additional energetic species such as reflected, neutralized gas atoms, atoms born in charge exchange collisions, and nonthermal sputtered atoms. All of them can participate in momentum transfer collisions with the background, cold atoms. These collisions are expected to be highly effective, due to the similar masses of the colliding partners. In this way, significant energy and momentum can be deposited from the energetic species to the background gas, giving rise to gas heating, and thereby

creating density inhomogeneity. These processes will also be treated in the present section.

3.6.1 Description of the Model

Species Included in the Model and Their Collision Processes

The present model is based on the general PIC-MCC algorithm, presented in the previous section, but some additional species are included, i.e., the fast argon atoms (Ar^f), sputtered copper atoms (Cu), singly ionized copper ions (Cu^+) and argon metastable atoms (Ar_m^*). The latter species are included, because they play an important role in ionization of the sputtered atoms. In addition, several new collision processes are added, such as electron-impact excitation to the Ar_m^* levels, and excitation and ionization from these Ar_m^* levels, quenching of the Ar_m^* levels by collisions with electrons or Ar atoms, electron–ion recombination, ionization of the sputtered Cu atoms by electron-impact, Penning ionization and asymmetric charge transfer. Details can be found in [144].

Besides these collision processes in the plasma, also some additional surface interactions are taken into account, such as sputtering and secondary electron emission caused by fast atoms and copper ions (Cu^+). Furthermore, deexcitation of the metastable argon atoms and recombination of the argon ions takes place at the walls. The energetic argon atoms are reflected and possibly thermalized at the walls. The coefficient of thermal accommodation, which is a measure for the energy exchange between energetic plasma species and the walls, has been chosen equal to 0.5.

Numerical Procedure

As it has been explained in the previous section, the PIC-MCC simulation needs to be run until a convergence is obtained. This numerical convergence must be correlated to the attainment of steady state by the real physical system that is the subject of the simulation. The time necessary for the physical system to reach a steady state is determined by the slowest processes in the system. When the heating of the gas is taken into consideration, the characteristic time, τ_H for thermal equilibrium (i.e., bringing the heat conduction to a steady state) is the longest: $\tau_H \sim 10^{-2}$ s. This estimate is based upon the relation [180]

$$\tau_H = \frac{L}{V_H} = \frac{c_p \rho L^2}{k}.$$

Here, L ($\simeq$0.1 m [101]) is the characteristic diffusion length, V_H ($= k/(\rho c_p L)$) is the characteristic speed of heat transfer, c_p is the specific heat per unit mass at constant pressure, ρ ($= 7.97 \times 10^{-5}$ kg m^{-3} [181]) is the argon mass density, k ($= 0.018$ W m^{-1} K^{-1} [181]) is the thermal conductivity of argon.

At the same time, the characteristic time for bringing electrons and ions to steady state does not exceed 10^{-5} s. All other important processes, such as the relaxation time for thermalization of the energetic neutrals and pressure equalization, are situated in between these two limits. Because of this big difference in the characteristic time steps of the electrons, ions, fast neutrals, and thermal conduction, some modifications in the general PIC-MCC algorithm are necessary to cope with this disparity. Not doing so would result in a huge amount of computational time. This is so, because of the general restriction for the time step (3.16) (see section "Stability and Accuracy of the PIC Model").

The procedure used here [182] is to advance the different sorts of particles with different time steps. The hierarchy being $\Delta t_e \ll \Delta t_i \ll \Delta t_n$ (with e = electron, i = ion, and n = neutral). This difference in the time steps is accounted for by the weight, W of the produced energetic, charge-exchange neutrals and sputtered atoms, i.e.,

$$W_n = W_s = W_i \frac{\Delta t_n}{\Delta t_i}, \tag{3.26}$$

where s refers to the sputtered atoms. Electrons are subcycled inside the ion time step (see section "Subcycling") and have $W_e = W_i$. In this way, it is assured that the production and loss rates of the real plasma particles are correctly represented, i.e., the global mass conservation is obeyed.

The procedure separates the particles into two groups, i.e., fast and slow. The upper size of the SPs from each group can be controlled independently from the corresponding value of the other group. When the upper limit is reached, only the members of the corresponding group are reduced twice, and their weight is doubled. The weight and number of the SPs from the other group are not changed. However, a change in the time step is needed, to maintain (3.26) to be valid. Because Δt_i is coherent with the stability criterion, the time step that always changes is $\Delta t_n (= \Delta t_s)$.

The overall cycle consists of one ion time step. At the end of this time step, the power, P, transferred to and from the feeding gas is accumulated

$$P = \frac{m_g W_n}{V_{cell} \Delta t_n} \left[\sum_l \frac{v'_l{}^2 - v_l{}^2}{2} - \sum_l \frac{v_l^2}{2} + \sum_l \frac{v'_l{}^2}{2} \right],$$

where v'_l is the post- and v_l the precollision velocity of the lth gas atom, m_g is the gas mass, V_{cell} is the volume of the computational grid cell. The first sum is the contribution from all collisions between the feeding gas atoms from one side and the ions, fast atoms, metastable atoms, and sputtered atoms from the other side. Only collisions, in which the postcollision energy of the gas atoms is less than some threshold, are counted. This threshold is chosen to be [182]

$$E_{th} = 9 \times 3/2 k_b T_g, \tag{3.27}$$

where k_b is the Boltzmann constant.

The other collisions result in creation of fast gas atoms, which are incorporated by the second sum. The third sum is the contribution of the thermalized fast gas atoms. This calculated power is used as a source term in the heat conduction equation

$$\frac{\partial^2 T_g}{\partial z^2} + \frac{1}{r}\frac{\partial}{\partial}\left(r\frac{\partial T_g}{\partial r}\right) = -\frac{P}{k}, \tag{3.28}$$

which is solved once per 10^{-8} s (actually, after each number of time steps divisible exactly by 100 and which sum is greater than or equal to 10^{-8} s) to calculate the gas temperature, T_g. In the above equation, k is the thermal conductivity of the gas.

It should be mentioned that T_g is a dynamic quantity dependent on the coordinates. Consequently the threshold energy given by (3.27) is also dynamic (changes with time) and is a function of the coordinates.

The sputtered atoms are followed as particles until being thermalized. Once that happens, they cannot anymore contribute to the gas heating directly; collisions between fast argon atoms and sputtered atoms are disregarded in the model, because of the statistical insignificance of the process. The overall copper density, however, is an important quantity for film deposition purposes. Therefore, a compromise between accuracy of the algorithm and its computational efficiency is to treat the thermalized copper atoms as a fluid. Thus, the overall copper density is a sum of the density of the fast copper atoms and the slow copper atoms. The density of the slow (thermalized) copper atoms, n_{Cu}^{sl}, can be obtained by solving the diffusion equation, which in (r, z) cylindrical coordinates reads

$$D_{Cu}\Delta n_{Cu}^{sl}(r,z) = r_{loss}(r,z) - r_{prod}(r,z), \tag{3.29}$$

where D_{Cu} is the diffusion coefficient of copper atoms in argon, r_{loss} is the rate of loss of the slow copper atoms, and r_{prod} is their production rate. The diffusion coefficient is taken to be, $D_{Cu} = 1.44 \times 10^{-2}\,\mathrm{cm^2\,s^{-1}}$ [183]. This value is based on the rigid-sphere collision model and refers to a pressure of 1 Torr and temperature of 300 K in argon.

The loss rate of the copper atoms, $r_{loss}(r, z)$, is equal to the rate of ionization of the copper atoms, caused by electron-impact, Penning ionization, and asymmetric charge transfer. The production rate of the copper atoms, $r_{prod}(r, z)$, is equal to the rate of thermalization of the sputtered atoms.

Equation (3.29), as well as (3.28), is mathematically the same as the Poisson equation for the potential. Therefore, the same numerical technique, i.e., cyclic reduction [154], is used for their solution. The boundary conditions of (3.29) are $\Delta n_{Cu}^{sl}|_{wall} = 0$ and $\nabla_r\left[n_{Cu}^{sl}(0,z)\right] = 0$. The latter represents simply the cylindrical symmetry of the system.

The procedure described above can be represented by the flowchart in Fig. 3.27.

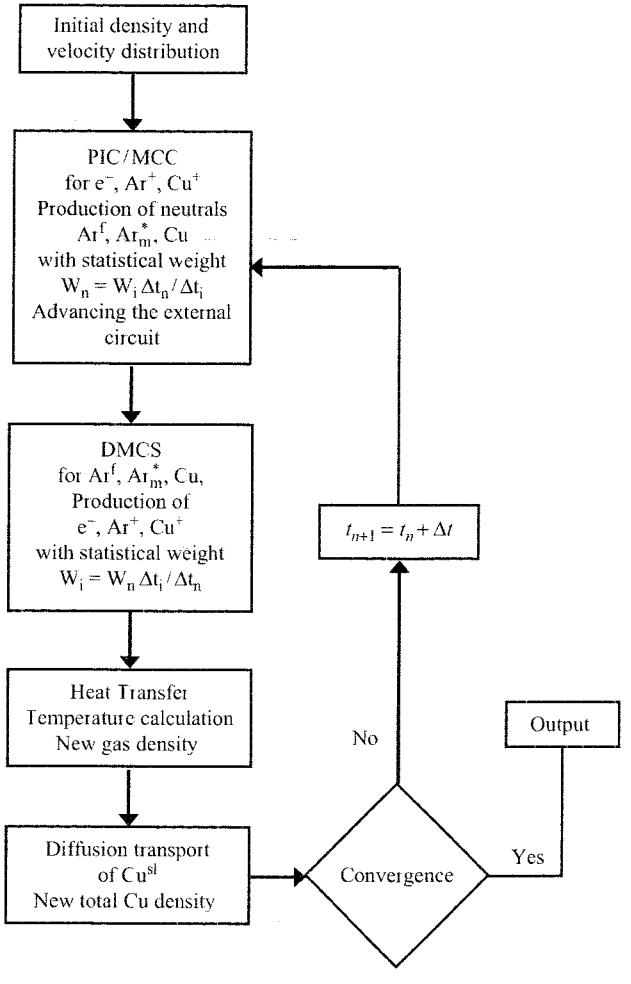

Fig. 3.27. Flowchart of the simulation procedure for calculation of the gas heating and the behavior of the sputtered (copper) species. The abbreviation DMCS stands for "Direct Monte Carlo simulation"

3.6.2 Examples of Calculation Results

The simulation procedure shown in Fig. 3.27 is applied to the magnetron discharge presented in Fig. 3.13. Simulations performed for pressures of 0.13, 0.53, 1.3, 3.3, 6.7, and 13 Pa, and for a maximum radial magnetic field above the cathode of 1,300 G, will be illustrated here. To verify the expected pressure dependence of the gas heating, the parameters of the external circuit (see section "External Circuit") have been readjusted in the course of the runs to maintain a constant power of 70 W.

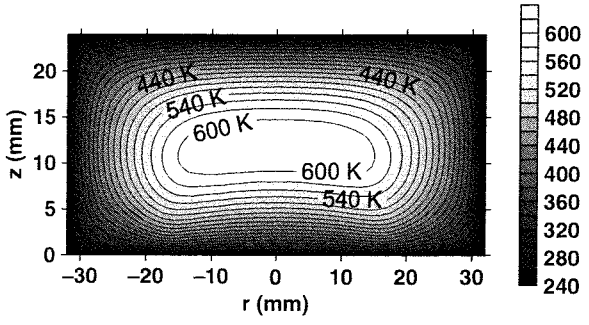

Fig. 3.28. Contour plot of the calculated gas temperature distribution at $p = 6.7$ Pa

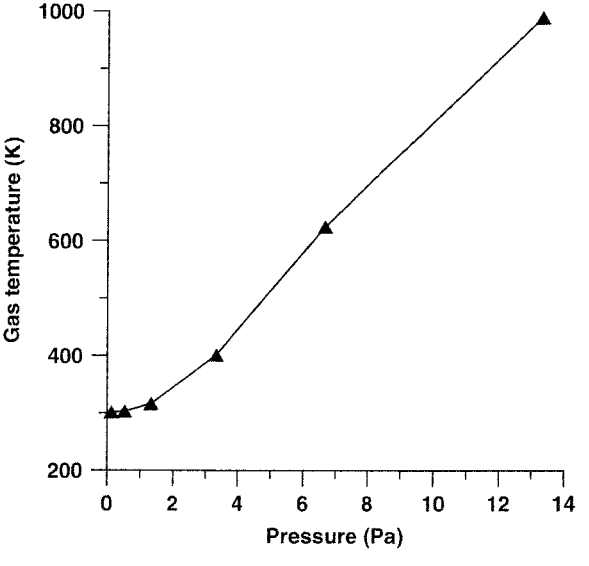

Fig. 3.29. Calculated maximum gas temperature as a function of the gas pressure at constant electric power of 70 W

Temperature Distribution

Figure 3.28 illustrates the calculated gas temperature distribution for the case of 6.7 Pa. The temperature reaches its maximum in the center of the discharge (both in axial and radial direction. The effect of gas pressure on the maximum gas temperature is plotted in Fig. 3.29. At 0.13 and 0.53 Pa, there is practically no heating of the gas. The rise of the gas temperature is about 1 K, which is within the limit of the expected calculation error. With the increase of the pressure, the gas begins to heat up. For $p = 1.3$ Pa, the temperature increases to 316 K, at 6.7 Pa, the maximum gas temperature is about 600 K (cf. also Fig. 3.28), and it reaching almost 1,000 K at 13 Pa.

Hence, it can be concluded that for the given operating conditions (argon gas, copper cathode, input power of 70 W), the gas heating is not significant for pressures of up to 1.3 Pa. These are typical conditions for laboratory magnetrons. Commercial sputtering magnetrons may be up to ten times bigger and with power supplies of several kW. These operating conditions, however, are outside the scope of this study. Indeed, PIC-MCC simulations would become too time-consuming for such large magnetron discharges (see also Sect. 3.3 above).

It is interesting to compare the obtained results with other data from the literature. The results for $p = 6.7$ Pa can be compared to [182], where the gas heating in a sputtering glow discharge is calculated for $p = 5.6$ Pa and 40 mm electrode separation. The temperature profile obtained there for a copper cathode and three times higher cathode voltage agrees very well with the gas temperature profile illustrated here. The lower voltage in the present case can be easily explained by the magnetic trap leading to much higher discharge efficiency, and to some extent with the smaller volume of the gas.

Another comparison can be made with [184], which is the most often cited work in the literature about the gas heating in sputter magnetrons. The author reports a density reduction of about 37% for a pressure of 4 Pa and a current of 300 mA. This corresponds reasonably well with our calculation results, in spite of the larger reactor geometry. Indeed, it can be deduced from Fig. 3.29 that the gas temperature at 4 Pa would be around 440 K, which is about 47% higher than 300 K.

More substantial is the difference with the calculations reported in the recent work of Epke and Dew [185]. The maximum temperature is on average a factor of two higher than the values presented here. In addition, the axial temperature profile is with a different shape. The values of the gas temperature in [185] are also higher than those in [184]. The shape of the profile in [185] resembles those obtained for analytical glow discharges in [186]. The common issue between these two models is that they are entirely or partially fluid. In addition, [185] is not a self-consistent simulation, but based on several assumptions, each of which brings uncertainties. The close correspondence of the absolute calculation values presented here, with the kinetic simulation [182] and the early experimental work [184] indicate that a kinetic self-consistent simulation represents more accurately the considered effect of gas heating in sputter magnetrons at typical operating conditions.

Density Profiles of the Other Plasma Species

The 2D density profile of the electrons (and Ar^+ ions) was already presented in section "Calculated Electron and Ar^+ Ion Densities" (Fig. 3.19). However, with the extended model, also the density profiles of the sputtered copper atoms, and the corresponding Cu^+ ions can be calculated, as well as the density profile of the Ar metastable atoms. Figure 3.30 presents the sputtered Cu atom density distribution at a pressure of 0.67 Pa. It shows a maximum at

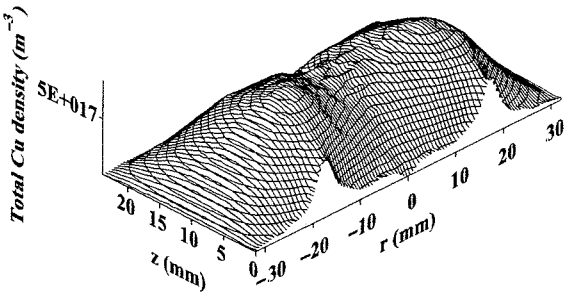

Fig. 3.30. Calculated sputtered Cu atom density

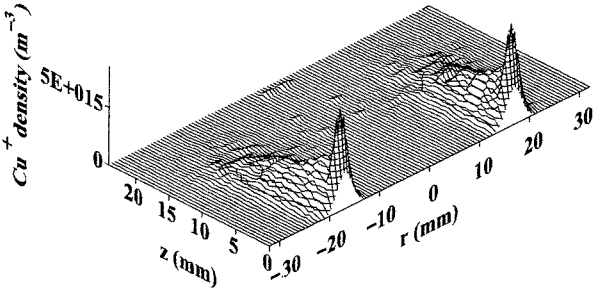

Fig. 3.31. Calculated Cu^+ ion density

$r = 18$ mm, where also the electron (and Ar^+ ion) density, the electron-impact ionization rate and hence the ion fluxes toward the cathode reached their maximum. Indeed, the ion flux gives rise to sputtering, hence most sputtering takes place at $r = 18$ mm, which explains the maximum in the sputtered Cu atom density. However, the peaks in the Cu atom density profile are definitely not so pronounced as in the electron density profile. This is because the Cu atom density profile is much more spread out by diffusion. It was found that at 0.67 Pa, a nonnegligible fraction of Cu atoms with energies of a few eV can reach the opposite wall of this magnetron discharge, where normally a substrate is mounted for deposition purposes. At higher pressures, however, the majority of the fast Cu atoms thermalize before reaching the anode [39].

The density profile of the corresponding Cu^+ ions is illustrated in Fig. 3.31. It is characterized by a very similar profile as the electrons and Ar^+ ions, but its density is clearly lower, so the main positive charge in the plasma is attributed to the Ar^+ ions.

Erosion Profile Due to Sputtering

Finally, the last calculation result shown here is the calculated erosion profile at the cathode, as a result of sputtering (see Fig. 3.32). Only one half of the axisymmetric target is shown. The erosion rate reaches its maximum at

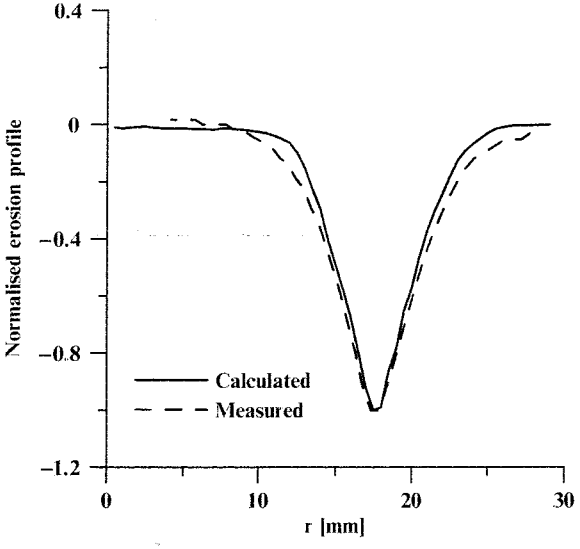

Fig. 3.32. Comparison of calculated (*solid line*) and measured (*dashed line*) normalized erosion profile

$r = 18\,\mathrm{mm}$, as expected. To verify the model, the calculated erosion profile is compared to a measured one at approximately the same operating conditions after 4 h of sputtering. The agreement is very satisfactory.

This demonstrates that the model captures the major physical processes of magnetron sputtering, including two-dimensional effects. Therefore, it can in principle be used to support experimental research, for instance for predicting how the target sputtering can be made more uniform and hence the target material can be consumed in a more efficient way.

3.7 Conclusions and Outlook for Future Work

In this chapter, we have given an overview of different modeling approaches developed for magnetron discharges, emphasizing their benefits and weaknesses. Furthermore, a two-dimensional self-consistent semi-analytical model and a two-dimensional PIC-MCC model are described in detail, and some examples of calculation results are presented. It was concluded that analytical approaches can give a very rapid prediction of certain discharge characteristics, but they are of course only valid under well-specified conditions. For a full description of the magnetron discharge, the PIC-MCC model is most appropriate, but it requires a very long computation time, which is acceptable for academic research, but unsuitable for industrial applications of sputter magnetrons. Nevertheless, the PIC-MCC simulations can give very useful insights,

to assist experimental work, and to provide a benchmark for the development of analytical models.

There is, however, still room for improvements and further developments of both models. The analytical model can be further improved by taking into account some processes which are neglected up to now, such as the self-consistent calculation of the electron temperature and the presheath, the electron contribution to the discharge current, and the effect of gas density reduction. Furthermore, by making minor, nonfundamental changes to the model, it could also be used to investigate aspects of the magnetron discharge, like the effect of the erosion groove formation on the target, or switching to another (nonreactive) discharge gas.

The PIC-MCC model, developed up to now, will also form a basis for further numerical studies. Indeed, the model is now only applicable to DC magnetrons in argon, but for the deposition of metal oxides and nitrides, reactive gas mixtures (argon–oxygen or argon–nitrogen) need to be used. Therefore, we plan to extend the PIC-MCC model, as presented here, to reactive gas mixtures, to predict the discharge behavior for reactive sputter-deposition purposes. Moreover, DC magnetrons often encounter problems when reactive gas mixtures are used, due to the deposition of nonconductive oxides or nitrides onto the cathode surface, and the subsequent charging issues of the cathode, leading to discharge failure. Therefore, we would also like to extend the current PIC-MCC model, developed for a DC magnetron, to pulsed magnetron discharges, so that the model will become more widely applicable to a range of operating conditions.

References

1. O. Yamazaki, K. Iyanagi, S. Takagi, K. Nanbu, Jpn. J. Appl. Phys. **41**(Part 1), 1230 (2002)
2. P. Pflug, N. Malkomes, V. Sittinger, B. Szyszka, in *45th SVC Annual Technical Conference Proceedings*, vol. 241, 2002
3. J. Kools, 47th SVC Annual Technical Conference Proceedings, vol. 31, 2004
4. U.H. Kwon, S.H. Choi, Y.H. Park, W.J. Lee, Thin Solid Films **475**, 17 (2005)
5. A.E. Wendt, M.A. Lieberman, H. Meuth, J. Vac. Sci. Technol. A **6**, 1827 (1988)
6. C.H. Shon, J.K. Lee, H.J. Lee, Y. Yang, T.H. Chung, IEEE Trans. Plasma Sci. **26**, 1635 (1998)
7. C.H. Shon, J.S. Park, B.K. Kang, J.K. Lee, Jpn. J. Appl. Phys. **38**(Part 1), 4440 (1999)
8. J. Kools, *Oral Presentation at 47th SVC Annual Technical Conference*, 2004
9. E. Shidoji, K. Ness, T. Makabe, Vacuum **60**, 299 (2001)
10. J.P. Biersack, L.G. Haggmark, Nucl. Instr. Methods **174**, 257 (1980)
11. W. Eckstein, *Computer Simulation of Ion-Solid Interactions* (Springer, Berlin Heidelberg New York, 1991)
12. J.F. Ziegler, Nucl. Instr. Methods Phys. Res. B **219–220**, 1027 (1991)
13. W. Möller, W. Eckstein, J.P. Biersack, Comp. Phys. Comm. **51**, 355 (1988)

14. W. Möller, M. Posselt, TRIDYN User Manual, 2002
15. M.A. Karolewski, Nucl. Instr. Methods Phys. Res. B **230**, 402 (2005). See also: http://www.geocities.com/karolewski/kalypso.htm
16. Y. Yamamura, M. Ishida, J. Vac. Sci. Technol. A **13**, 101 (1995)
17. N. Matsunami, Y. Yamamura, Y. Itikawa, N. Itoh, Y. Kazumata, S. Miyagawa, K. Morita, R. Shimizu, H. Tawara, At. Data Nucl. Data Tables **31**, 1 (1984)
18. J.E. Mahan, A. Vantomme, J. Vac. Sci. Technol. A **15**, 1976 (1997)
19. M. Stephanova, S.K. Dew, J. Vac. Sci. Technol. A **19**, 2805 (2001)
20. K.T. Kuwata, R.I. Erickson, J.R. Doyle, Nucl. Instr. Methods Phys. Res. B **201**, 566 (2003)
21. A.M. Myers, J.R. Doyle, D.N. Ruzic, J. Appl. Phys. **72**, 3064 (1992)
22. T. Nakano, S. Baba, Thin Solid Films, **343–344**, 24 (1999)
23. T. Smy, L. Tan, S.S. Winterton, S.K. Dew, M.J. Brett, J. Vac. Sci. Technol. A **15**, 2847 (1997)
24. K. Macàk, P. Macàk, U. Helmersson, Comp. Phys. Comm. **120**, 238 (1999)
25. S. Mahieu, G. Buyle, D. Depla, S. Heirwegh, P. Ghekiere, R. De Gryse, Nucl. Instr. Methods Phys. Res. B **243**, 313 (2005)
26. S. Hong, E. Kim, B.-S. Bae, K. No, J. Vac. Sci. Technol. A **14**(5), 2721 (1996)
27. D.B. Graves, M.J. Kushner, J. Vac. Sci. Technol. A **21**, S152 (2003)
28. W. Jacobs, A. Kersch, J. Vac. Sci. Technol. A **21**, 922 (2003)
29. G.H. Gilmer, H. Huang, T.D. de la Rubia, J. Dalla Torre, F. Baumann, Thin Solid Films **365**, 189 (2000)
30. T.S. Cale, T.P. Merchant, L.J. Borucki, A.H. Labun, Thin Solid Films **365**, 152 (2000)
31. V. Vyas, M.J. Kushner, J. Vac. Sci. Technol. A **25**, 1955 (2006)
32. M.M.M. Bilek, D.R. McKenzie, Czech. J. Phys. **52**(Suppl. D), 905 (2002)
33. T. Hammerschmidt, A. Kersch, P. Vogl, Phys. Rev. B **71**, 205409 (2005)
34. I. Petrov, P.B. Barna, L. Hultman, J.E. Greene, J. Vac. Sci. Technol. A **21**, S117 (2003)
35. S. Mahieu, G. De Winter, D. Depla, R. De Gryse, J. Denul, Surf. Coat. Technol. **187**, 122 (2004)
36. T.A. van der Straaten, N.F. Cramer, I.S. Falconer, B.W. James, J. Phys. D: Appl. Phys. **31**, 177 (1998)
37. I. Kolev, A. Bogaerts, R. Gijbels, Phys. Rev. E **72**, 056402 (2005)
38. I. Kolev, A. Bogaerts, IEEE Trans. Plasma. Sci. **34**, 886 (2006)
39. I. Kolev, A. Bogaerts, Plasma Processes Polym. **3**, 127 (2006)
40. S.M. Rossnagel, H.R. Kaufman, J. Vac. Sci. Technol. A **5**, 2276 (1987)
41. L. Gu, M.A. Lieberman, J. Vac. Sci. Technol. A **6**, 2960 (1988)
42. A.E. Wendt, Ph.D. thesis, University of California at Berkeley, 1988
43. A.E. Wendt, M.A. Lieberman, J. Vac. Sci. Technol. A **8**, 902 (1990)
44. F. Guimaraes, J. Almeida, J. Bretagne, J. Vac. Sci. Technol, A **9**, 133 (1991)
45. T. Miura, Jpn. J. Appl. Phys. **39**(Part 1), 4890 (2000)
46. L. Pekker, Plasma Sources Sci. Technol. **4**, 31 (1995)
47. K. Wasa, S. Hayakawa, *Handbook of Sputter Deposition Technology: Principles, Technology, and Applications* (Noyes, Park Ridge, NJ, 1992)
48. N.F. Cramer, J. Phys. D: Appl. Phys. **30**, 2573 (1996)
49. A. Palmero, E.D. van Hattum, W.M. Arnoldbik, F.H.P.M. Habraken, Surf. Coat. Technol. **188–189**, 392 (2004)
50. J.W. Bradley, G. Lister, Plasma Sources Sci. Technol. **6**, 524 (1997)

51. J.W. Bradley, Plasma Sources Sci. Technol. **7**, 572 (1998)
52. J.W. Bradley, R.D. Arnell, D.G. Armour, Surf. Coat. Technol. **97**, 538 (1997)
53. W. Möller, D. Güttler, B. Abendroth, R. Grötzschel, *Invited Presentation at BELVAC Symposium on Reactive Sputter Deposition*, Ghent, Belgium, 2006
54. G. Buyle, W. De Bosscher, D. Depla, K. Eufinger, J. Haemers, R. De Gryse, *Vacuum* **70**, 29 (2003)
55. G. Buyle, D. Depla, K. Eufinger, J. Haemers, R. De Gryse, W. De Bosscher, J. Vac. Sci. Technol. A **21**, 1218 (2003)
56. G. Buyle, D. Depla, K. Eufinger, R. De Gryse, J. Phys. D: Appl. Phys. **37**, 1639 (2004)
57. G. Buyle, D. Depla, K. Eufinger, J. Haemers, W. De Bosscher, R. De Gryse, *Vacuum* **74**, 353 (2004)
58. F.F. Chen, *Introduction to Plasma Physics Controlled Fusion* (Plenum Press, New York, 1964)
59. J.W. Bradley, Plasma Sources Sci. Technol. **5**, 622 (1996)
60. M. Rabinski, in *ICPP & 25th EPS Conference on Controlled Fusion Plasma Physics*, ECA vol. 22C, 1998, p. 2165
61. R. Krimke, H.M. Urbassek, Plasma Sources Sci. Technol. **5**, 389 (1996)
62. G. Lister, J. Vac. Sci. Technol. A **14**, 2736 (1996)
63. S.T. Surzhikov, J.S. Shang, J. Comput. Phys. **199**, 437 (2004)
64. C. Costin, L. Marques, G. Popa, G. Gousset, Plasma Sources Sci. Technol. **14**, 168 (2005)
65. B. Kuvshinov, E. Westerhof, T. Schep, M. Berning, Phys. Lett. A **241**, 287 (1998)
66. E. Passoth, J.F. Behnke, C. Csambal, M. Tichý, P. Kudrna, Yu.B. Golubovskii, I.A. Porokhova, J. Phys. D: Appl. Phys. **32**, 2655 (1999)
67. I.A. Porokhova, Yu.B. Golubovskii, J. Bretagne, M. Tichy, J.F. Behnke, Phys. Rev. E **63**, 056408 (2001)
68. I.A. Porokhova, Yu.B. Golubovskii, C. Csambal, V. Helbig, C. Wilke, J.F. Behnke, Phys Rev. E **65**, 046401 (2002)
69. I.A. Porokhova, Yu.B. Golubovskii, M. Holík, P. Kudrna1, M. Tichý, C. Wilke, J.F. Behnke, Phys. Rev. E **68**, 016401 (2003)
70. I.A. Porokhova, M. Holík, O. Bilyk, P. Kudrna, Yu.B. Golubovskii, M. Tichý, J.F. Behnke, Contrib. Plasma Phys. **45**, 319 (2005)
71. I.A. Porokhova, Yu.B. Golubovskii, J.F. Behnke, Phys. Rev. E **71**, 066406 (2005)
72. I.A. Porokhova, Yu.B. Golubovskii, J.F. Behnke, Phys. Rev. E **71**, 066407 (2005)
73. Yu.B. Golubovskii, I.A. Porokhova, V.P. Sushkov, M. Holík, P. Kudrna, M. Tichý, Plasma Sources Sci. Technol. **15**, 228 (2006)
74. I. Porokhova, Private communication
75. T.E. Sheridan, M.J. Goeckner, J. Goree, J. Vac. Sci. Technol. A **8**, 30 (1990)
76. T.E. Sheridan, M.J. Goeckner, J. Goree, J. Vac. Sci. Technol. A **8**, 1623 (1990)
77. J.E. Miranda, M.J. Goeckner, J. Goree, T.E. Sheridan, J. Vac. Sci. Technol. A **8**, 1627 (1990)
78. M.J. Goeckner, J. Goree, T.E. Sheridan, IEEE Trans. Plasma Sci. **19**, 301 (1991)
79. J. Goree, T.E. Sheridan, Appl. Phys. Lett. **59**, 1052 (1991)
80. J. Li, Q. Chen, Z. Li, J. Phys. D: Appl. Phys., 1995, **28**, 681 (1995)

81. J. Li, Q. Chen, Z. Li, J. Phys. D: Appl. Phys. **28**, 1121 (1995)
82. J. Li, Q. Chen, W. Zhang, Z. Li, J.J. Pan, J. Phys. D: Appl. Phys. **29**, 1624 (1996)
83. C. Heise, K. Lemke, M. Kock, Contrib. Plasma Phys. **37**, 431 (1997)
84. Q.H. Fan, J.J. Gracio, L.Q. Zhou, J. Appl. Phys. **95**, 6017 (2004)
85. S. Ido, K. Nakamura, Jpn. J. Appl. Phys. **32**(Part 1), 5698 (1993)
86. S. Ido, K. Nakamura, Vacuum **47**, 1035 (1996)
87. S. Ido, K. Nakamura, Jpn. J. Appl. Phys. **35**(Part 1), 2302 (1996)
88. M. Kashiwagi, S. Ido, Vacuum **53**, 33 (1999)
89. S. Ido, M. Kashiwagi, M. Takahashi, Jpn. J. Appl. Phys. **38**(Part 1), 4450 (1999)
90. S. Ido, T. Suzuki, M. Kashiwagi, Jpn J. Appl. Phys. **37**(Part 1), 965 (1998)
91. E. Shidoji, M. Nemoto, T. Nomura, Y. Yoshikawa, Jpn J. Appl. Phys. **33**, 4281 (1994)
92. E. Shidoji, M. Nemoto, T. Nomura, J. Vac. Sci. Technol. A **18**, 2858 (2000)
93. A. Lopp, C. Braatz, M. Geisler, H. Claus, J. Trube, in *45th SVC Annual Technical Conference Proceedings*, vol. 170, 2002
94. Q.H. Fan, L.Q. Zhou, J.J. Gracio, J. Phys. D: Appl. Phys, **36**, 244 (2003)
95. T. Kubart, R. Novak, J. Valter, Czech. J. Phys. **54**(Suppl. C), 1027 (2004)
96. G. Buyle, D Depla, J. Haemers, W. De Bosscher, R. De Gryse, in *SVC 48th Annual Technical Conference Proceedings*, Denver, Colorado, vol. 254, 2005
97. K. Nanbu, S. Kondo, Jpn. J. Appl. Phys. **36**, 4808 (1997)
98. W. Zhu, G. Buyle, J. Lopez, S. Shanmugmurthy, A. Belkind, K. Becker, R. De Gryse, New J. Phys. **8**, 146 (2006)
99. A.M. Myers, J.R. Doyle, J.R. Abelson, D.N. Ruzic, J. Vac. Sci. Technol. A **9**, 614 (1991)
100. C. Eisenmenger-Sittner, R. Beyerknecht, A. Bergauer, W. Bauer, G. Betz, J. Vac. Sci. Technol. A **13**, 2435 (1995)
101. V. Serikov, K. Nanbu, J. Vac. Sci. Technol. A **14**, 3108 (1996)
102. O. Yamazaki, K. Iyanagi, S. Takagi, K. Nanbu, Jpn. J. Appl. Phys. **41**, 1230 (2002)
103. B. Feddes, J.G.C. Wolke, J.A. Jansen, A.M. Vredenberg, J. Appl. Phys **93**, 662 (2003)
104. A. Kuzmichev, I. Goncharuk, IEEE Trans. Plasma Sci. **31**, 994 (2003)
105. U.H. Kwon, W.J. Lee, Jpn. J. Appl. Phys. **45**, 8629 (2006)
106. A. Bogaerts, R. Gijbels, W.J. Goedheer, J. Appl. Phys. **78**, 2233 (1995)
107. R.K. Porteous, D.B. Graves, IEEE Trans. Plasma Sci. **19**, 204 (1991)
108. R.K. Porteous, H.-M. Wu, D.B. Graves, Plasma Sources Sci. Technol. **3**, 25 (1994)
109. E. Shidoji, N. Nakano, T. Makabe, Thin Solid Films **351**, 37 (1999)
110. E. Shidoji, H. Ohtake, N. Nakano, T. Makabe, Jpn. J. Appl. Phys. **38**, 2131 (1999)
111. E. Shidoji, E. Ando, T. Makabe, Plasma Sources Sci. Technol. **10**, 621 (2001)
112. I. Kolev, A. Bogaerts, Contrib. Plasma Phys. **44**, 582 (2004)
113. K. Ness, T. Makabe, Phys. Rev. E **62**, 4083 (2000)
114. E. Shidoji, T. Makabe, Thin Solid Films **442**, 27 (2003)
115. R.L. Kinder, M.J. Kushner, J. Vac. Sci. Technol. A **19**, 76 (2001)
116. S. Kondo, K. Nanbu, J. Phys. D: Appl. Phys. **32**, 1142 (1999)
117. A. Vetushka, J.W. Bradley, J. Phys. D: Appl. Phys. **40**, 2037 (2007)

118. C.K. Birdsall, A.B. Langdon, *Plasma Physics via Computer Simulations* (Adam Hilger, Bristol, 1991)
119. T.A. van der Straaten, N.F. Cramer, I.S. Falconer, B.W. James, J. Phys. D: Appl. Phys. **31**, 191 (1998)
120. K. Nanbu, S. Segawa, S. Kondo, Vacuum **47**, 1013 (1996)
121. S. Kondo, K. Nanbu, J. Vac. Sci. Technol. A **19**, 830 (2001)
122. T.M. Minea, J. Bretagne, G. Gousset, L. Magne, D. Pagnon, M. Touzeau, Surf. Coat. Technol., **116–119**, 558 (1999)
123. J.P. Verboncoeur, A.B. Langdon, N.T. Gladd, Comp. Phys. Comm. **87**, 199 (1995)
124. C. Birdsall, Homepage of The Plasma Theory and Simulation Group: http://ptsg.eecs.berkeley.edu/
125. Y. Kusumoto, K. Iwata, Vacuum **74**, 359 (2004)
126. Y. Miyagawa, M. Ikeyama, S. Miagawa, H. Nakadate, Nucl. Instr. Methods Phys. Res. B **206**, 767 (2003)
127. Y. Miyagawa, H. Nakadate, M. Tanaka, M. Ikeyama, S. Miyagawa, Surf. Coat. Technol. **196**, 155 (2005)
128. S. Kuroiwa, T. Mine, T. Yagisawa, T. Makabe, J. Vac. Sci. Technol. B **23**, 2218 (2005)
129. T. Yagisawa, T. Makabe, J. Vac. Sci. Technol. A **24**, 908 (2006)
130. G. Buyle, Ph.D. Thesis, University of Ghent, Belgium, 2005
131. M.D. Bowden, T. Nakamura, K. Muraoka, Y. Yamagata, B.W. James, M. Maeda, J. Appl. Phys. **73**, 3664 (1993)
132. K. Kuwahara, H. Jujiyama, IEEE Trans. Plasma Sci. **22**, 442 (1994)
133. A. Pflug, B. Szyszka, V. Sittinger, J. Niemann, in *46th SVC Annual Technical Conference Proceedings*, vol. 241, 2003
134. D. Depla, S. Heirwegh, S. Mahieu, J. Haemers, R. De Gryse, J. Appl. Phys. **101**, 013301 (2007)
135. J. Bareilles, G.J.M. Hagelaar, L. Garrigues, C. Boniface, J.P. Boeuf, Phys. Plasmas, **11**, 3035 (2004)
136. A. Smirnov, Y. Raitses, N.J. Fisch, Phys. Plasmas, **11**, 4922 (2004)
137. J. Bohlmark, U. Helmersson, M. VanZeeland, I. Axnäs, J. Alami, N. Brenning, Plasma Sources Sci. Technol., **4**, 654 (2004)
138. P. Kudrna, M. Holik, M. Tichy, C. Csambal, J.F. Behnke, Czech. J. Phys. **52**(Suppl. D), 666 (2002)
139. K. Nanbu, IEEE Trans. Plasma Phys. **28**, 971 (2000)
140. K. Nanbu, Phys. Rev. E **55**, 4642 (1997)
141. K. Nanbu, Phys. Rev. E **56**, 7314 (1997)
142. J.A. Thornton, J. Vac. Sci. Technol. **15**(2), 171 (1978)
143. D. Depla, G. Buyle, J. Haemers, R. De Gryse, Surf. Coat. Technol. **200**, 4329 (2006)
144. I. Kolev, Ph.D. Thesis, University of Antwerp, Belgium, 2007
145. F.S. Acton, *Numerical Methods That Work* (Mathematical Association of America, Washington, 1990)
146. J.P. Boris, in *Proceedings Fourth Conference Numerical Simulation of Plasmas*, vol. **3** (Naval Research Laboratory, Washington DC, 1970)
147. C.K. Birdsall, D. Fuss, J. Comput. Phys. **3**, 494 (1969)
148. R.W. Hockney, J.W. Eastwood, *Computer Simulations Using Particles* (Adam Hilger, Bristol, 1988)

149. P.K. MacKeown, D.J. Newman, Computational Techniques in Physics (Adam Hilger, Bristol, 1987)
150. E. Brigham, *Fast Fourier Transform and Its Applications* (Prentice-Hall, Upper Saddle River, NJ, 1988)
151. P.N. Swartztrauber, SIAM J. Numer. Anal. **11**, 1136 (1974)
152. C.K. Birdsall, W.B. *Bridges, Electron Dynamics of Diode Regions* (Academic, New York, 1966)
153. C.K. Birdsall, A.B. Langdon, *Plasma Physics via Computer Simulations* (Adam Hilger, Bristol, 1991)
154. J.P. Verboncoeur, M.V. Alves, V. Vahedi, C.K. Birdsall, J. Comput. Phys **104**, 321 (1993)
155. V. Vahedi, G. DiPeso, J. Comput. Phys. **131**, 149 (1996)
156. R.W. Hamming, *Digital Filters* (Dover, Mineola, NY, 1998)
157. D. Schlichthärle, *Digital Filters: Basics and Design* (Springer, Berlin Heidelberg New York, 2000)
158. E. Kawamura, C.K. Birdsall, V. Vahedi, Plasma Sources Sci. Technol. **9**, 413 (2000)
159. K. Nanbu, J. Phys. Soc. Jpn. **49**, 2042 (1980)
160. A. Matveev, Mol. Phys., Vyshaya Shkola, Moscau (1987)
161. W. Feller, *An Introduction to Probability Theory and Its Applications*, vol. 2, (Wiley, New York, 1971)
162. H.R. Scullerud, Brit. J. Appl. Phys. Ser. 2 **1**, 1567 (1968)
163. V. Vahedi, M. Surendra, Comput. Phys. Commun **87**, 179 (1995)
164. K. Nanbu, Jpn. J. Appl. Phys. **33**, 4752 (1994)
165. Y.P. Raizer, *Gas Discharge Physics* (Springer, Berlin Heidelberg New York, 1997)
166 K.J. Bowers, J. Comput. Phys. **173**, 393 (2001)
167 W.H. Press, S.A. Teukolsky, W.T. Vetterling, B.P. Flannery, *Numerical Recipes in Fortran, The Art of Scientific Computing* (Cambridge University Press, Cambridge, 1992)
168. T.H. Cormen, C.E. Leiseron, R.L. Rivest, *Introduction to Algorithms* (MIT Press, Cambridge, MA, 1990)
169. E. Eggarter, J. Chem. Phys. **62**, 883 (1975)
170. M. Hayashi, IPPJ-AM Research Rep. 19 (unpublished) Available on:ftp://jila.colorado.edu/collision_data/electronneutral/hayashi.txt
171. A.V. Phelps, Petrovic, Z. Lj, Plasma Sources Sci. Technol. **8**, R21 (1999)
172. A.V. Phelps, J. Phys. Chem. Ref. Data **20**, 557 (1991)
173. A.V. Phelps, J. Appl. Phys. **76**, 747 (1994)
174. J.W. Bradley, S. Thompson, Y. Aranda Gonzalvo, Plasma Sources Sci. Technol. **10**, 490 (2001)
175. A. Bogaerts, R. Gijbels, J. Appl. Phys. **78**, 6427 (1995)
176. F.F. Chen, in *Plasma Diagnostics Technics*, ed. By R.H. Huddlestone, S.L. Leonard,(Academic, New York, 1965)
177. D.J. Field, S.K. Dew, R.E. Burrell, J. Vac. Sci. Technol. A **20**, 2032 (2002)
178. P. Spatenka, J. Vlcek, J. Blazek, Vacuum, **55**, 165 (1999)
179. T.E. Sheridan, M.J. Goeckner, J. Goree, J. Vac. Sci. Technol. A **9**, 688 (1991)
180. I.P. Bazarov, *Thermodynamics* (Pergamon Press, New York, 1964)
181. R.L. Powell, G.E. Childs, in *American Institute of Physics Handbook*, ed. by D.E. Grey, (McGraw-Hill, New York, 1972)

182. V. Serikov, K. Nanbu, J. Appl. Phys. **82**, 5948 (1997)
183. J.O. Hirschfelder, C.F. Curtiss, R.B. Bird, *Molecular Theory of Gases and Liquids* (Wiley, New York, 1964)
184. S.M. Rossnagel, J. Vac. Sci. Technol. A **6**, 19 (1988)
185. S.D. Epke, S.K. Dew, J. Phys. D: Appl. Phys. **39**, 1413 (2006)
186. A. Bogaerts, R. Gijbels, V. Serikov, J. Appl. Phys. **87**, 8334 (2000)